Author:
Stefanski, Taryn V

Title:
Investigating spinterferometry

first order coherence of charged quantum dots

INVESTIGATING SPINTERFEROMETRY: FIRST ORDER COHERENCE OF CHARGED QUANTUM DOTS

Taryn Victoria Stefanski

A dissertation submitted to the University of Bristol in accordance with the requirements for award of the degree of Master of Science in the Faculty of Science, School of Physics.

August 2020

Word Count: 17400

Declaration

I declare that the work in this dissertation was carried out in accordance with the requirements of the University's *Regulations and Code of Practice for Research Degree Programmes* and that it has not been submitted for any other academic award. Except where indicated by specific reference in the text, the work is the candidate's own work. Work done in collaboration with, or with the assistance of, others, is indicated as such. Any views expressed in the dissertation are those of the author.

SIGNED: DATE:

Copyright ©

Abstract

In recent years, quantum technologies have become a rich area of research and development. Semiconductor platforms, namely quantum dots, have been proposed as a potential solution to applications including quantum computing, quantum memory, and single photon sources. In this thesis, we examine the coherence properties of the electron in a charged InGaAs quantum dot sample within a photonic micropillar cavity. We take advantage of the deterministic light-matter interaction between photons and the electron in the quantum dot in order to probe spin dynamics and coherence properties by interfering photons that have scattered off of the two-level system, and we examine the visibility of the resulting interference fringes. We will show how significant background noise from the probing laser may convolute visibility measurements to the extent that the expected profile from the quantum dot changes. Furthermore, we will examine phonon interactions as one of the dominant dephasing mechanisms that arises in these systems, as well as investigate how the spin state can be manipulated with ultrafast laser pulses with a specific polarization. Long coherence times and control of the quantum state are imperative for maintaining stable superposition states, entanglement, and performing quantum logic gates, required for quantum computing.

Acknowledgements

There are many individuals to whom I owe a debt of gratitude for challenging, motivating, and supporting me throughout my past year in Bristol. First and foremost, I would like to thank my supervisors Professor Ruth Oulton and Dr. Edmund Harbord, especially for their patience, understanding, and support as I tackled this research endeavor and for helping me develop as a physicist and researcher. Additionally, I would like to thank Professor John Rarity for the stimulating discussions provided in our board and weekly meetings. I would also like to thank Dr. Dara McCutcheon for his insights and assistance with the theoretical aspects of my research. I am also grateful for all of the members of the quantum dot research group and the camaraderie among the team. In particular, I owe many thanks to Andrew Young and Joseph Lennon for their immense help in the lab and the office answering my countless questions. Thank you to Andrew, specifically, for supervising my lab work and helping to proofread my thesis, and to Joe for the numerous invaluable discussions. I also owe many thanks to my undergraduate research supervisor, Professor Johannes Pollanen, for his continuous support and for giving me my first look into the world of quantum engineering research. Finally, I would like to thank my family, especially my parents, friends, and partner for their never-ending support, reassurance, and comedic relief.

Contents

List of Figures and Tables

Figures

Tables

List of Abbreviations

APD – avalanche photodiode

BS – beam splitter

CB – conduction band

CCD – charge-coupled device

CP – circularly polarized

CW – continuous wave

DBR - distributed Bragg reflector

HWP – half wave plate

LA – longitudinal acoustic

LP – linear polarizer (in experimental diagrams)

LP – linearly polarized (in Chapter 5)

MZ – Mach-Zehnder

PBS – polarizing beam splitter

PMF – polarization maintaining fiber

PSB – phonon sideband

QD – quantum dot

QWP – quarter wave plate

SMF – single mode fiber

STIRAP – Stimulated Raman adiabatic passage

TLS – two-level system

VB – valence band

ZPL – zero-phonon line

Chapter 1

Introduction

1.1 Thesis overview

In this thesis, we will focus on investigation of the first order coherence of a single electron in a charged In(Ga)As quantum dot sample within a photonic micropillar cavity. These semiconductor structures have been recognized for their potential application in quantum information processing due to their substantial coherence times and isolation from the environment. However, the optical two-level system and spin of the electron are still prone to sources of decoherence. We will look at decoherence of the quantum dot in the weak scattering regime in order to better understand the dephasing. This is important for use of these systems for quantum memory storage, as well as implementing well-defined single qubit gates. We also set out to show preparation of the electron spin in a steady state via first order coherence measurements, moving towards the demonstration of coherent control. The following is a detailed outline of my thesis.

This chapter, Chapter 1, provides an introduction to quantum dots in terms of their physical structure and uses. We begin by explaining what quantum dots are and why spins and the spin-photon interface are important, as well as provide a brief discussion of some potential applications. Then, we discuss the fabrication process and provide the details of the specific sample used to conduct the experiments described in later chapters. Additionally, we explain the selection rules allowing for optical access of the quantum dot's states.

Chapter 2 will discuss commonly practiced experimental techniques in the study of quantum dots. We explain photoluminescence, coherent scattering, and interferometry, as well as the first and second order correlation functions. Photoluminescence is used to classify quantum dots based on their emission energies and select them accordingly. Coherent scattering and interferometry are described as the basis of the experimental procedures utilized in each reported experiment. Coherent scattering describes the manner of the spin-photon interaction and interferometry is used to measure the first order coherence. Finally, we discuss the first and

second order correlation functions, commonly used measurements in the field. We discuss how the first order correlation function is related to visibility, which can be extracted from the interferometer and is presented throughout the thesis to quantify the coherence properties of the quantum dot.

Chapter 3 will focus on characterization of the interferometer. We present the expected form of the visibility due to coherent scattering from neutral and charged quantum dots with and without an applied magnetic field. Then, we examine how the qualitative shape of the visibility envelope is altered when various amounts of background light from the laser are introduced. The findings reported are important for analyzing and understanding future measurements.

Chapter 4 will consider the phonon sideband of our charged sample and how it compares to neutral and charge tunable quantum dots in different cavity structures. Because longitudinal acoustic phonons are a primary cause of dephasing of the optical coherence of the two-level system in quantum dots, even at low temperatures, it is advantageous to investigate the degree of their effect and the time scale on which it occurs. Understanding and mitigating this source of decoherence can aid in increasing collection of coherent emission of indistinguishable photons. We present measurements of the first order coherence to look at the coherence time of the phonon interactions and the percent of their contribution to photon emission at various excitation powers.

Chapter 5 will focus on coherent control of the electron spin in the charged quantum dot sample. The ability to coherently control the spin state of the excess electron on ultrafast time scales using a pulsed, optical laser has gained attention as a way to implement numerous qubit gates within the decoherence time of the system. Although we do not perform initialization of the spin and we collect time averaged measurements of the first order coherence, we find that it is possible to prepare the spin in a steady state aligned with the applied magnetic field with sufficient pulsed laser power and polarization specific pulses.

Overall, in the experimental chapters (3-5) we will discuss, mainly qualitatively, the first order coherence function of our charged quantum dot sample. These results are obtained using interferometry in order to extract information about the coherence of the two-level system and spin dynamics of the electron.

1.2 Quantum dots

1.2.1 What are quantum dots?

Quantum dots (QD) are zero-dimensional solid-state semiconductor structures on the nanometer scale that can be practically implemented in the field of quantum optics as artificial atoms. In a semiconductor structure, there exists a valence band (VB) and a conduction band (CB) separated by a region of forbidden electron energies, collectively called the bandgap. Electrons reside in the valence band and can be optically or electrically excited into the conduction band, as depicted in Figure 1.1. The absorption of a photon with sufficient energy (greater than or equal to the bandgap energy) allows the excitation to proceed. The promoted electron leaves a hole (with charge +e) in its place in the VB. The electron can decay radiatively back into the VB, recombining with the hole and producing a photon in the process. Typically, in these QDs, this process happens on the order of 1 ns and the process by which it produces a photon is called fluorescence.

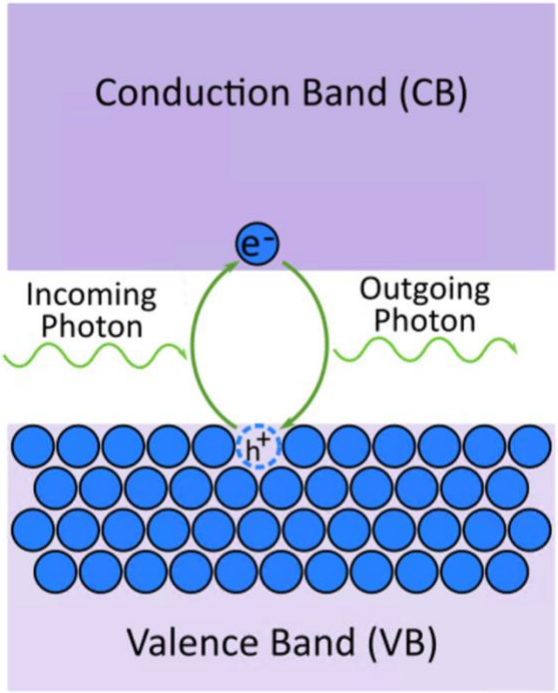

Figure 1.1. Semiconductor band structure. The solid, blue circles are electrons, whereas the circle with the blue, dashed outline is a hole. When the electron is optically excited by an incoming photon, it moves to the conduction band, leaving behind a positively charged hole in its place in the valence band. It may recombine with the hole to emit a photon.

In a quantum dot, the electron and hole are bound together via the confining potential within the quantum dot and Coulomb attraction [1]. The pairing of the electron and hole forms a quasiparticle called an exciton. The quantum dots are created by imbedding a semiconductor with a small bandgap into one with a larger bandgap, creating a 3D potential well. Commonly used are III-V semiconductors, such as GaAs and InAs, as they have a direct bandgap. The length of the potential well in each direction is on the scale of the de Broglie wavelength of the electron ($\lambda = h/p$) where p is the linear momentum and h is Planck's constant. This results in quantum confinement, where motion is restricted and quantized in all three directions. Another result of this phenomenon is modification of the density of states, where in a quantum dot the allowed energy levels become discrete, giving them the name "artificial atoms" [2].

The envelope wave functions and allowed energies of the electron within the quantum dot can be modeled using the "particle in a box" solution, commonly known in quantum mechanics, since there is confinement in all three directions. We can assume that the potential outside of the box is infinite, and zero within the walls of the box. We define the length and width of the box, which are equal, as "a," and the height as "b." We begin with the standard form of the time independent Schrödinger equation in 3D:

$$\frac{-\hbar^2}{2m_{eff}}\nabla^2\psi(\vec{r}) = E\psi(\vec{r}) \tag{1.1}$$

Here, $\hbar$ is Planck's constant, m_{eff} is the effective mass of the hole or electron, depending on if the calculation is for the valence or conduction band, $\psi(\vec{r})$ is the 3D envelope wave function, and E is the energy of the electron. The Schrödinger equation can be separated into each of the three components, but here we show the x component as an example:

$$\frac{-\hbar^2}{2m_{eff}}\frac{\partial^2}{dx^2}\psi(x) = E\psi(x) \tag{1.2}$$

As aforementioned, the solution to this problem is well known in quantum mechanics, so we can write the total wavefunction and energy, as well as these expressions for each individual component. When writing it for each component, we only need to change the quantum number, coordinate, and length variable, but the general form remains the same. We denote the principal

quantum number in the x direction as "n," "m" in the y direction, and "l" in the z direction. For x we get the following wavefunction and energy:

$$\psi(x) = \sqrt{\frac{2}{a}} sin\left(\frac{n\pi x}{a}\right) \tag{1.3}$$

$$E_x = \frac{\hbar^2}{2m_{eff}}\left(\frac{n\pi}{a}\right)^2 \tag{1.4}$$

The expressions for the total wavefunction and energy in all three directions are:

$$\psi(\vec{r}) = \sqrt{\frac{8}{a^2 b}} sin\left(\frac{n\pi x}{a}\right) sin\left(\frac{m\pi y}{a}\right) sin\left(\frac{l\pi z}{b}\right) \tag{1.5}$$

$$E_{total} = \frac{\hbar^2\pi^2}{2m_{eff}}\left[\left(\frac{n}{a}\right)^2 + \left(\frac{m}{a}\right)^2 + \left(\frac{l}{b}\right)^2\right] \tag{1.6}$$

When n = m = l = 1, the electron is in the ground state. Increasing either n or m by 1 reveals information about the next excited state. The energy difference between the two states is given by:

$$\Delta E = \frac{3\hbar^2\pi^2}{2m_{eff}a^2} \tag{1.7}$$

We use the values a=20 nm, b= 5 nm, and m_{eff} of the electron (used in calculations for the conduction band) equals 0.063*m_e, m_{eff} of the hole (used in calculations for the valence band) equals 0.51*m_e, where m_e is the rest mass of a free electron ($9.11*10^{-31}$ kg). The ratios for the effective masses are for electrons and heavy holes within gallium arsenide, obtained from the semiconductor database from the Ioffe Institute [3]. Plugging in values, we get a separation energy of ΔE = 44.7 meV in the conduction band and ΔE = 5.5 meV in the valence band. The exact values obtained may vary depending on the exact size of the quantum dot and the values of the effective masses used, but this calculation serves to show the relevant orders of magnitude. At room temperature (~300 K) phonons are present and have an energy of ~25 meV, which is sufficient to excite a hole to the next excited state. In order to avoid this, the quantum dot sample is cooled using liquid helium to ~4.2 K, where phonons only supply ~0.36 meV of energy [4]. Although this energy is enough to cause some dephasing to the two-level system, it will not

cause unwanted excitation. In terms of size, we find that a few 10s of nm in length/width is the most appropriate for the QD as increasing this size by an order of magnitude would drastically reduce the energy level separation, allowing excitation via phonons even at low temperatures.

So far, we have only considered a neutral exciton. However, it is possible to obtain a charged exciton, also known as a trion, if an excess electron is present in the CB and permanently resides there. It has been proposed that this electron can be utilized as a spin qubit in order to implement gates and perform quantum computation [5]. Various hardware platforms have been proposed for potential use in quantum computing including trapped ions, superconducting circuits, and NV centers in diamond [6]. However, electrons in semiconductor quantum dots are attractive because the electron spin is well isolated due to the confinement created by the QD and has a relatively long coherence time which would be beneficial for storing quantum memory and performing a large number of gate operations. The electron spins can be controlled optically or by electrically gating and coupling two quantum dots [5, 7]. The motivation for this thesis is to gain a deeper understanding of the decoherence mechanisms and spin control of these systems so that they can eventually be utilized for quantum computation.

A qubit, or quantum bit, is the quantum mechanical analogue to a bit used in classical computation. However, quantum computation exploits uniquely quantum mechanical phenomena including superposition and entanglement, and this is what gives it the potential to be such a powerful computational tool [6, 8]. In classical computation, a bit can exist in one of two states, either a $|0\rangle$ or a $|1\rangle$. Whereas a qubit requires two, fundamental basis states but may exist in a superposition of the two states until measurement, when the state collapses. The state of the qubit takes the form of $\alpha|0\rangle + \beta|1\rangle$ – a linear combination of the basis states. The coefficients α and β are restricted by the normalization relation $|\alpha|^2 + |\beta|^2 = 1$, and $|\alpha|^2$ and $|\beta|^2$ are the probabilities of obtaining $|0\rangle$ or $|1\rangle$, respectively, when the state is measured. As a result of this property, the power of a quantum computer scales exponentially, meaning it can store 2^n quantum states given n qubits [8]. The state of a qubit can be manipulated by applying a quantum logic gate, which can be mathematically represented by a unitary matrix. Additionally, entanglement involves two or more qubits whose states are highly correlated with one another. In a general sense, measurement of one qubit reveals information indicative of the quantum state of the other qubit(s) if they were to be measured. However, the decoherence time of a qubit restricts the ability to observe both superposition and entanglement. Decoherence would cause the

unwanted loss of the phase relationship between the components of the superposition state, and would inhibit entanglement.

DiVincenzo defines five conditions that must be met in order to realize quantum computation which are a system of well-defined qubits (in this case, electron spins), deterministic initialization of the quantum state, low decoherence, responsive to unitary transformations, or gates, and finally, accurate measurements of the quantum state or read out [5]. The solid-state structure of a quantum dot makes it an attractive system due to potential scalability, as well as ease of integration with cavities and optical components which is beneficial for control, storage, and detection of the quantum state. However, because of the solid-state environment, both the spin and two-level system are prone to sources of decoherence, namely fluctuating nuclear spins in the heterostructure, and phonon interactions [7].

Photons, on the other hand, are another attractive qubit candidate as they can propagate significant distances with very little coherence loss and information can be encoded in polarization or path. However, scalability poses a serious limitation as there is a lack of means to store the information encoded in the states for a substantial amount of time. A popular area of research is an approach that integrates the two, using a light-matter interface with the electron spin acting as a "stationary" qubit and the photon acting as a "flying" qubit. Essentially, information can be encoded in the spin of the electron and in the polarization or mode of the photon, and it is necessary to have a way in which the two can accurately transfer information between one another.

Many quantum technologies require single photon sources, including quantum key distribution, linear optical quantum computing, and quantum metrology [9]. Ideally, one wants a single photon source that has a high efficiency and that can reliably produce one photon at a time that is indistinguishable from other emitted photons so that they are able to interfere [10]. Utilizing quantum dots as a single photon source seems intuitive due to the discrete nature of photon emission and the ability to trigger fluorescence with an optical or electrical stimulus. Additionally, coupling with a microcavity enhances both indistinguishability and efficiency of the QD.

On the applications front, Lindner and Rudolph (2009) have proposed a protocol using quantum dots to generate linear "cluster states" composed of a long chain of entangled photons, which could be utilized for quantum computing. This is accomplished by taking advantage of the

spin of the electron in a QD and triggering photon emission at various points during its precession. If the electron has a long coherence time, this imparts less error on the photons, which would need to be corrected if used for quantum computing. Additionally, it is beneficial to operate in a low magnetic field so that the electron spin undergoes minimal rotation whilst the radiative decay is occurring [11]. In order to accomplish this task, it is vital to have a controllable, well-behaved spin that can be measured. In this thesis we utilize the interference of photons that have deterministically interacted with the quantum dot electron spin in order to probe the spin dynamics in our sample imbedded within a micropillar cavity. We do this in order to retrieve information about its spin state and decoherence due to phonons.

1.2.2 Growth technique and sample details

As aforementioned, quantum dots provide spatial confinement of the resident exciton in three dimensions. The most common way of fabricating these semiconductor nanostructures is using the Stranski-Krastanov growth method [12]. This technique requires the use of molecular beam epitaxy so that layers of semiconductor can be deposited individually. Our sample is composed of the III-V semiconductors InAs and GaAs, where InAs has a substantially smaller bandgap and is hosted within a GaAs substrate, allowing for confinement within the structure. First, layers of GaAs are deposited, followed by the deposition of InAs, which forms the wetting layer. Due to the 7% lattice mismatch between the two layers, once the layer of InGaAs reaches a critical thickness, accumulated strain is relieved through the random formation of nanoscale droplets [13]. Quantum dots generated in this manner are commonly referred to as "self-assembled" for this reason. After formation of the 3D structure, more GaAs is deposited as a capping layer. A diagram of the growth process is displayed in Figure 1.2. Growth conditions including temperature and composition ratio can affect the size, shape, and emission wavelength of the quantum dot. These types of QDs are composed of ~10^5-10^6 atoms and have a size on the scale of a few to 10s of nanometers in each direction and emit photons with wavelengths typically in the range 850-1000 nm. Quantum dots can be selected based on the desired optical properties necessary for coupling into a cavity or generating single photons with a certain wavelength. Additionally, if the substrate has a sufficiently low density of quantum dots ($<10^9/cm^2$), the QDs can more easily be isolated and incorporated into cavities, making the study of single QDs more straightforward.

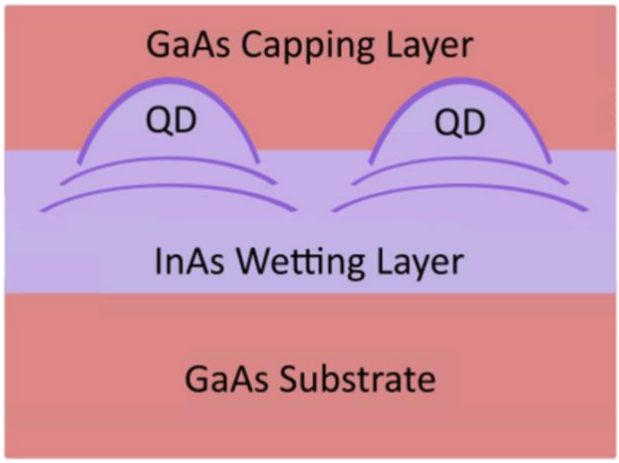

Figure 1.2. Stranski-Krastanov growth of quantum dot sample. InAs is deposited atop a GaAs substrate layer and once it reaches a critical thickness, droplets form and these are our quantum dots. The purple lines indicate where the InAs layer has relieved strain by forming the islands. Finally, the QDs are capped with additional GaAs.

As aforementioned, the presence of an excess electron spin confined within a quantum dot can be functionally realized as a spin qubit. The existence of an excited, trion state allows for optical manipulation of the excess electron spin, as will be discussed later in this thesis. It is possible to create charge-tunable quantum dots in which the charge state is manipulated by an externally applied bias voltage via a Schottky diode [14]. However, the spin state is more stable when the sample is permanently charged, resulting from n-type delta doping. This method is used in the fabrication of our sample, where silicon is the dopant material. During the deposition of semiconductor layers with molecular beam epitaxy, a layer of silicon is deposited below the In(Ga)As layer. One of the donor electrons from the silicon may subsequently become trapped within the quantum dot's potential well, residing in the conduction band and permanently charging the QD.

The sample utilized for each experiment described in the remainder of this thesis consists of a modulation doped In(Ga)As quantum dot imbedded within a low-Q-factor micropillar cavity (~290). The Q factor is a quantity that indicates the ratio of the emission energy of the cavity mode, compared to the linewidth [15]. The quantum dot has a diameter of ~10 nm and the cavity ~2 μm. The structure is composed of a λ-thick cavity with $\lambda/4$-thick distributed Bragg reflectors (DBR) on top and bottom, acting as highly reflective mirrors. The materials that make up the DBRs have different refractive indices, causing partial reflection at each boundary. Because each

layer is $\lambda/4$-thick, this results in constructive interference of the reflected waves within the cavity. The ability of the DBRs to reflect incident waves depends on the number of mirror pairs making up the cavity. In our cavity, the DBRs are made from AlAs/GaAs mirror pairs with 5 and 18 on top and bottom, respectively, causing stronger reflectivity from the bottom.

Utilizing a micropillar cavity provides a multitude of experimental benefits. The structure allows localization of the light in three dimensions, provides well-defined directionality for the emission process making collection easier, and offers ease of integration with other optical components [16]. The micropillar cavity aids in directing light emission into one specific cavity mode, decreasing loss into leaky modes. It has also been shown that the spontaneous emission rate of the QD is enhanced when the emission frequency is resonant with the cavity mode via the Purcell effect, and suppressed when photon emissions are off-resonance [17]. Another result of the Purcell effect is the reduction in the radiative lifetime of the exciton. It is possible to reduce this time below the dephasing time and improve indistinguishability of emitted photons, as a result. A faster radiative lifetime also means a speed up in the repetition rate so that generation of single photons can be prompted more rapidly [18]. Additionally, it has been demonstrated experimentally that coupling with these cavities augments efficient production and collection of single photons [19, 20]. We leave this discussion about micropillar cavities relatively brief as with our specific cavity, we do not observe significant cavity quantum electrodynamic effects nor a strong Purcell enhancement since it has a low-quality factor. The main advantage of using it in our experiments is to provide a well-defined direction for the emitted light.

1.2.3 Selection rules

As aforementioned, it is possible to optically excite an electron from the VB to the CB given that sufficient energy is used. However, this excitation is conditional on certain selection rules dictated by the intrinsic spin of the electrons and the orbital-like characteristics of the valence and conduction bands. Although neutral and charged quantum dots are governed by different selection rules, we focus on the explanation of selection rules of a charged system since we only use a negatively charged quantum dot in the experiments presented later.

Electrons are spin 1/2 particles and holes act as the positively charged analogue. As such, they have spins of $\pm\frac{1}{2}$ where these values are the spin projections along the growth/optical axis,

which we define as the z-axis. The conduction band has an s-like orbital and therefore, an orbital angular momentum of $\ell = 0$, giving the electrons a total angular momentum of $\pm\frac{1}{2}$. On the other hand, the valence band has a p-like orbital, so the holes occupy states with an orbital angular momentum of $\ell = 1$. We use $|J, J_z\rangle$ to denote the total angular momentum and its respective component along the z-axis. We see heavy holes with $\left|\frac{3}{2}, \pm\frac{3}{2}\right\rangle$, light holes with $\left|\frac{3}{2}, \pm\frac{1}{2}\right\rangle$, and a split-off band with $\left|\frac{1}{2}, \pm\frac{1}{2}\right\rangle$. The split-off band is lower in energy by 100s of meV and due to strain in the z direction, the light holes are 10s of meV lower in energy as compared to the heavy hole and can be neglected [21].

In the Faraday geometry, or basis of the optical (z) axis, ground state electrons can only be excited to the trion states via circularly polarized transitions in which the photon imparts one quanta of light with an angular momentum of ± 1. The spin-up(down) electrons have a total angular momentum of + $\frac{1}{2}$ (- $\frac{1}{2}$) and the spin-up(down) holes have a total angular momentum of + $\frac{3}{2}$ (- $\frac{3}{2}$), so a photon with an angular momentum of +1(-1) is required to drive the transition. Cross transitions are forbidden because this would require a change in angular momentum of +/- 2. The transition is also governed by the spin of the resident electron in the conduction band. Due to the Pauli exclusion principle, the electron arising from the photoexcitation must have a spin anti-aligned with the other electron. When in the first excited state, the electrons exist in a spin singlet configuration. Spin-up electrons (+ $\frac{1}{2}$) are depicted as $|\uparrow\rangle$, spin-down electrons (- $\frac{1}{2}$) as $|\downarrow\rangle$, spin-up holes (+ $\frac{3}{2}$) as $|\Uparrow\rangle$, and spin-down holes (- $\frac{3}{2}$) as $|\Downarrow\rangle$.These transitions are depicted in Figure 1.3(a).

However, applying a magnetic field in the Voigt geometry (defined by a magnetic field perpendicular to the growth axis), along the x-axis and in plane with the QD, we change the allowed transitions and generate two lambda systems as both vertical and cross transitions are optically accessible. A lambda system is one in which a single excited state is coupled to two ground states, and when drawn in a diagram resembles the Greek letter lambda. This allows for coupling of the two ground states via one of the trion states. By our convention, vertical transitions are achieved using vertically polarized light along the y axis, perpendicular to both the field and optical axes. Cross transitions are achieved with horizontally polarized light,

parallel to the magnetic field, and are out of phase with the vertical transitions by $\pi/2$, indicated by i. These transitions are pictured in Figure 1.3(b). The spin states are in the x-basis where $|\uparrow/\downarrow\rangle_x = \frac{1}{\sqrt{2}}(|\uparrow\rangle_z \pm |\downarrow\rangle_z)$. Additionally, there is non-zero splitting between the two ground and two excited states due to the application of the magnetic field. The Zeeman splitting is proportional to the magnitude of the field and causes each of the transitions to require differing amounts of energy.

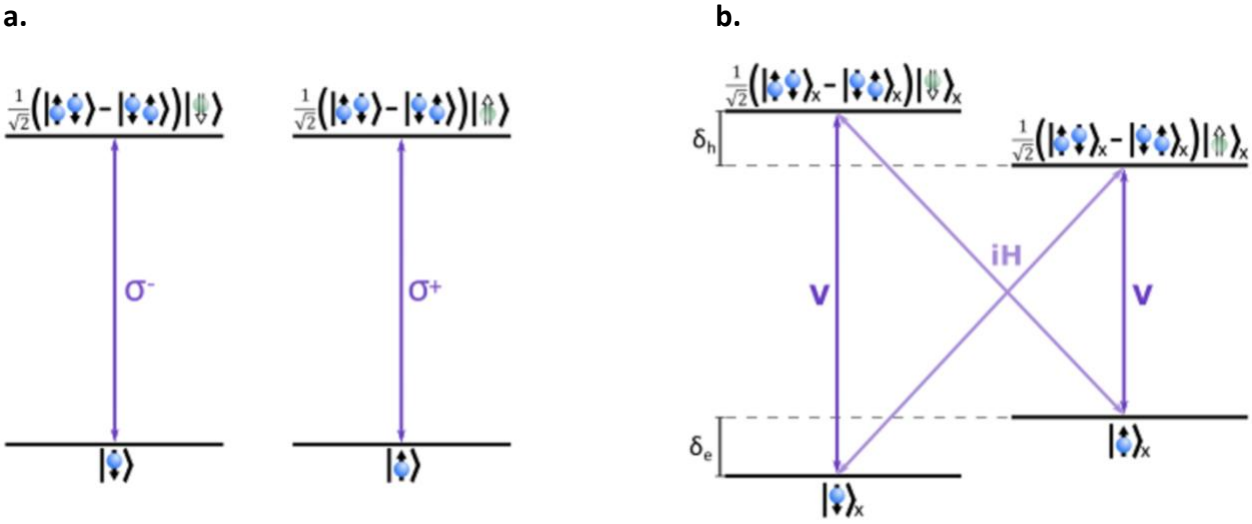

Figure 1.3. Optical selection rules for a charged quantum dot. **a.** Allowed optical transitions in the basis of the optical (z) axis, or Faraday geometry. Cross transitions are not allowed and vertical transitions occur with circularly polarized light where σ^+ is the left-handed circular polarization and σ^- corresponds to the right-handed circular polarization. **b.** Allowed optical transitions in the basis of the Voigt geometry where a magnetic field is applied along the x-axis. Cross and vertical transitions are allowed where V indicates vertically polarized light, and H indicates horizontally polarized light. The i indicates a phase factor of $\pi/2$. Zeeman splitting of electrons and holes is indicated by δ_e and δ_h, respectively.

These selection rules are especially relevant for our optical experiment involving coherent control, which will be presented later in Chapter 5, in which we use the Voigt geometry to exploit the two lambda systems generated.

Chapter 2

Experimental methods

In this chapter, we will look at common experimental techniques used in the classification and analysis of quantum dots and their optical properties. We begin with a general description of photoluminescence, which is used to identify and select quantum dots based on emission energies. The subsequent two sections, coherent scattering and interferometry, are directly relevant to the experiments whose results are presented in chapters 3-5. Finally, the concluding sections pertain to significant measurements utilized in the field.

2.1 Photoluminescence

Photoluminescence is a routine technique used to characterize quantum dots based on their emission energies. This can be used to select individual quantum dots with the desired wavelength. This is done by using a laser as a light source to excite electrons from the valence band to the conduction band of the semiconductor structure via absorption of a photon. During this process, a hole is left in the valence band. The photon must have an energy greater than or equal to the bandgap energy of the quantum dot, E_{QD} in Figure 2.1, in order for excitation to occur.

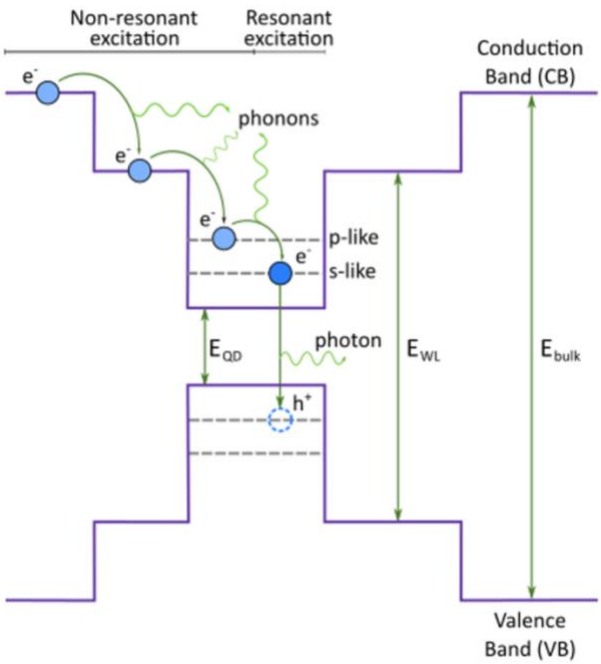

Figure 2.1. Bandgap structure and emission diagram of In(Ga)As quantum dots. The upper and lower structures represent the conduction and valence bands, respectively, in the growth direction. From right to left are the bandgap energies of the bulk semiconductor (GaAs), E_{Bulk}, the wetting layer with a reduced bandgap labelled E_{WL}, and finally, the bandgap of the quantum dot, itself, E_{QD}. Arrows between electrons indicate decay into lower energy levels, accompanied by phonon emission, and the arrow between the electron (e^-) and hole (h^+) demonstrates exciton recombination with photon emission.

It is possible for a photon with sufficient energy to excite an electron into the wetting layer or bulk semiconductor. Following this non-resonant excitation, the electrons will relax into the lowest possible state of the conduction band. The loss of energy of the electron is compensated for by the accompanying emission of phonons. An analogous process happens with holes, as well, where they are created in the valence band by the lack of electron and relax towards the top of the valence band. The relaxation of both the electron and hole is necessary to form an exciton. These decay processes occur on a timescale much shorter than the radiative lifetime of the exciton. When the electron has relaxed to the minimum energy state, the exciton can radiatively recombine due to spontaneous emission, producing a photon in the process. The emitted photons are collected and fed into a spectrometer to produce an energy spectrum, allowing for analysis of the emission energies, typically close to the bandgap energy of the QD [2]. Performing photoluminescence measurements on a large array of QDs, or an ensemble,

produces a broad, Gaussian shaped energy spectrum, as different QDs may have different emission energies due to the various sizes and strains. Masks with small apertures can be used to spatially select QDs, and discrete emission energy lines become apparent as fewer QDs are optically probed [22].

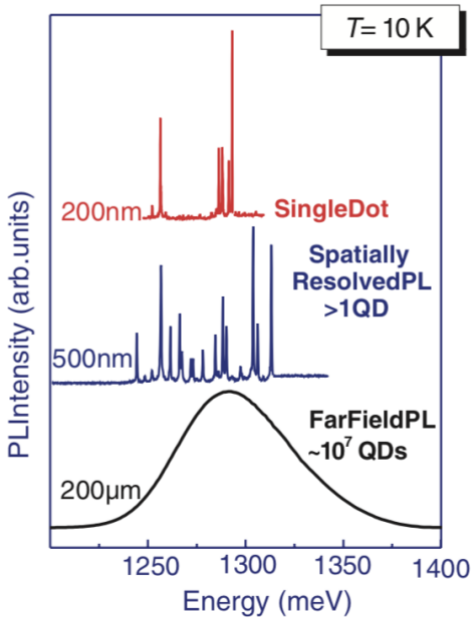

Figure 2.2. Photoluminescence spectra of quantum dot(s) using masks with holes of various sizes (200 nm, 500nm, and 200 um). The smaller the size of the aperture, the fewer the number of dots that are optically accessed, which exhibit discrete emission lines. Reprinted from "A review of the coherent optical control of the exciton and spin states of semiconductor quantum dots," by A.J. Ramsay, 2010, *Semiconductor Science and Technology*, *25*(10). Copyright 2010 by IOP Publishing Ltd.

2.2 Coherent scattering

It is also possible to perform resonant excitation by tuning the wavelength of the laser to or very close to the transition frequency. Collecting the resonance fluorescence signal from a quantum dot is important in the measurement of various optical properties. Because the wavelength of the fluorescence and scattered photons from the laser are the same, one cannot distinguish them spectrally, so polarization or spatial discrimination are commonly used. As compared to non-resonant excitation, the indistinguishability of photons emitted from the quantum dot acting as a single photon source is improved when utilizing resonant excitation. This method helps to mitigate the presence of additional energy in the surrounding semiconductor lattice, and

therefore, helps to reduce the influence of dephasing mechanisms on the exciton, such as phonon interactions.

When the quantum dot is driven on resonance, the emission is composed of a coherent and an incoherent fraction, the ratios of which depend on the driving power. At low powers, or in the weak excitation regime, coherent scattering dominates, and real excitation is highly suppressed. As implied by the name, coherent scattering is a coherent process in which the photons are elastically scattered off of the two-level system (TLS) and retain phase information with respect to the other scattered photons. Coherent scattering can be used to generate and obtain single photons from a quantum emitter. However, as the power of the light field interacting resonantly with the quantum dot increases, the number of real excitations prevails. These real excitations lead to incoherent fluorescent emission [23].

In the case of a neutral quantum dot, scattered photons retain the coherence properties of the laser [23]. As a result, the first order coherence demonstrates an extremely long coherence time as compared with the coherence time of the exciton within the quantum dot. Matthiesen et al. (2012) reports a coherence time 15 times longer than the coherence time of spontaneously emitted photons, and 30 times longer than the radiative lifetime of the exciton [24]. However, when a measurement of the second order correlation is performed, a dip towards zero is evident at $\tau = 0$, confirming that the light is still quantum in nature which is a direct result of interaction with the TLS [24, 25].

2.3 Interferometry

Interferometry is an important experimental practice used to generate an interference pattern that may reveal information about a light source, in this case our charged quantum dot, over a finite period of time. Each experiment detailed in the following chapters requires the use of a Mach-Zehnder (MZ) interferometer, depicted in Figure 2.3. In a general sense, interference is caused by splitting the amplitude of a light wave at a beamsplitter, introducing a relative phase shift between the two paths by changing the length of one, and recombining the waves at a second beamsplitter to observe the resulting interference effects, or visibility fringes. Essentially, this means interfering two separate sections of the photon wave packet. From this, we can extract information about spin dynamics in the case of a charged quantum dot, and the first order

coherence, as interference fringes are only observed for light that is coherent [2, 26]. We explain visibility and the concept of coherence in more detail in the next section.

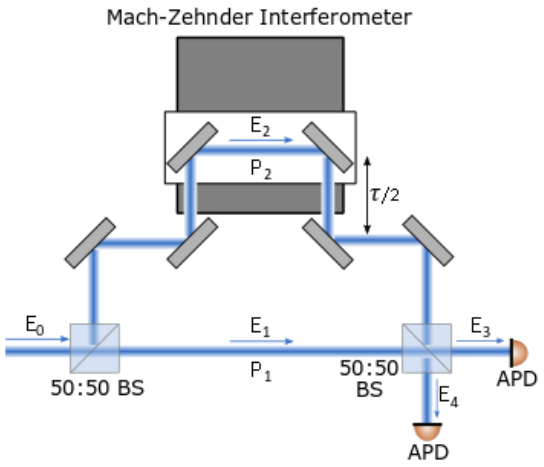

Figure 2.3. Physical set up of Mach-Zehnder interferometer used in all experiments. E_0 is incoming light wave, P_1 and P_2 are path lengths, τ is the time delay caused by the translation stage, BS is beamsplitter, and APD is avalanche photodiode that records photon counts.

In our set up, seen in Figure 2.3, the light that enters the MZ interferometer, labeled E_0, is split by a 50:50 beam splitter (BS) into two separate paths, E_1 and E_2. In this section (2.3), E refers to the electric field of a light wave, not to be confused with E for energy, exclusively used in section 2.2. The top path, followed by E_2, introduces a variable time delay (τ) via a motorized translation stage (coarse delay) and a fine scanning piezo (fine delay). The piezo (not pictured) applies various voltage biases to sweep through one wavelength at a given value of τ. Then, the two light waves are recombined at another 50:50 beamsplitter and detected by one of two avalanche photodiodes (APD) depending on the constructive or destructive nature of the light. We will see that photon detection oscillates between the two APDs and that is why the visibility fringes are sinusoidal. We can derive a general mathematical description of the intensity of light at each of the APDs via the following analysis [27].

Let $E_0(t) = E_0 e^{-i\omega t}$ be the original, incoming light wave. We let it take the form of a monochromatic carrier wave for the purpose of this analysis. The first beamsplitter splits the wave into two components:

$$E_1(t) = E_2(t) = \frac{E_0(t)}{\sqrt{2}} = \frac{E_0}{\sqrt{2}} e^{-i\omega t} \tag{2.1}$$

The two waves traverse different paths. As a result, upon recombination at the second beamsplitter, E_1 is a function of t, where t is the time it takes to traverse P_1, and E_2 is a function of t + τ, where τ is the variable time delay added when the stage is moved and is the time corresponding to $\frac{P_2-P_1}{c}$. The variables P_1 and P_2 are the physical path lengths of each arm of the interferometer, corresponding to E_1 and E_2, respectively (see Figure 2.3), and c is the speed of light. The difference between P_1 and P_2 determine the relative phase between the two light waves. The final phase difference between the two paths when recombined at the second beamsplitter also depends on the number of reflections off mirrors and beamsplitters, each of which introduces an extra pi phase shift. As such, the two waves are out of phase by π when registered at the APD collecting E_3, corresponding with destructive interference, and the two waves are in phase at the APD collecting E_4, so there is constructive interference.

The output electric fields are written as follows:

$$E_3(t) = \frac{1}{\sqrt{2}}\left(\frac{E_0}{\sqrt{2}}e^{-i\omega t} - \frac{E_0}{\sqrt{2}}e^{-i\omega(t+\tau)}\right)$$

$$= \frac{E_0}{2}e^{-i\omega t}(1 - e^{-i\omega\tau}) \tag{2.2}$$

$$E_4(t) = \frac{1}{\sqrt{2}}\left(\frac{E_0}{\sqrt{2}}e^{-i\omega t} + \frac{E_0}{\sqrt{2}}e^{-i\omega(t+\tau)}\right)$$

$$= \frac{E_0}{2}e^{-i\omega t}(1 + e^{-i\omega\tau}) \tag{2.3}$$

Because intensity is proportional to $|E|^2$ and we take the time average:

$$I_{3/4} \propto \langle (E_{3/4})^* (E_{3/4}) \rangle$$

$$I_3 \propto E_0^2 sin^2(\frac{\omega\tau}{2})$$

$$I_4 \propto E_0^2 cos^2(\frac{\omega\tau}{2}) \tag{2.4}$$

Here we have shown a detailed derivation of the intensities which we will see in the next section can be used to calculate the visibility and subsequently the coherence time. We see from the sinusoidal terms that collection of the light by the APDs oscillates between the two detectors. In practice we collect the number of photon counts over a specified time interval, which is proportional to intensity. We refer to interferometry where we collect light that has interacted with a charged quantum dot sample as spinterferometry, as the visibility spectrum can elucidate information about the spin of the electron including how fast it decoheres. This measurement is at the core of all of our experiments.

2.4 First order correlation function

A light wave can be characterized by the fixed phase relationship between the wave and itself at a different point in time or space. This property is called coherence and can be quantified in the spatial or temporal domain. We focus on the time domain in which we can quantify this property by coherence time, τ_c. Knowing the phase of the light wave at some arbitrary starting time, we can predict the phase at a later time with high certainty if the latter time is within the coherence time, and minimal certainty if the latter time has surpassed the coherence time.

It is possible to extract the coherence time from a measurement of the first order correlation function, or $g^{(1)}(\tau)$. This is also known as an amplitude correlation as it measures how well two fields can interfere with one another, as interference is only possible if the fields are coherent. Additionally, it is called "first order" because it is dependent on the measurement of one field, or one photon from a quantum mechanical perspective. It can also be called an auto-correlation measurement because the field is interfering with a later version of itself. We measure the first order correlation function by putting a signal through a Mach-Zehnder interferometer where the wave is split into two components and later recombined after one component (E_2 in Figure 2.3) has experienced some time delay, τ, with respect to the other component (E_1 in Figure 2.3). This will ultimately reveal the coherence time of the light wave. We measure the first order correlation as a function of time delay. The function is defined as:

$$g^{(1)}(\tau) = \frac{\langle E^*(t)E(t+\tau)\rangle}{\langle |E(t)|^2\rangle} \tag{2.5}$$

Where the brackets $\langle ... \rangle$ indicate time averaging. Ideally, we expect $g^{(1)}(\tau) = 1$ when $\tau = 0$, indicating perfect coherence. The coherence decays to zero as $e^{-\tau/\tau_c}$ [2].

In the experiments detailed in later chapters, we plot and analyze the **visibility**. This refers to the visibility of the sinusoidal interference fringes, acquired by contrasting the high and low intensities registered at each detector. This can be obtained directly from the interferometer and easily related to the first order correlation function. We begin with the formula for visibility:

$$v = \frac{I_4 - I_3}{I_4 + I_3} \tag{2.6}$$

The intensities of the output fields of the MZ interferometer, calculated in the previous section are as follows:

$$I_3 \propto \langle |E_0(t)|^2 \rangle - Re\langle E_0^*(t) E_0(t+\tau) \rangle$$

$$I_3 \propto E_0^2 sin^2(\frac{\omega\tau}{2}) \tag{2.7}$$

$$I_4 \propto \langle |E_0(t)|^2 \rangle + Re\langle E_0^*(t) E_0(t+\tau) \rangle$$

$$I_4 \propto E_0^2 cos^2(\frac{\omega\tau}{2}) \tag{2.8}$$

The intensity subscripts are used to differentiate the intensities at each output and are consistent with those used in section 2.3, and E_0 indicates the monochromatic light wave we used previously. The proportionality constants excluded from equations (2.7) and (2.8) can be disregarded when calculating the visibility because they are scaling factors that ultimately cancel out. Additionally, we arrive at equations 2.7 and 2.8 by assuming the terms $\langle |E_0(t)|^2 \rangle$ and $\langle |E_0(t+\tau)|^2 \rangle$ are equal as they equate to the intensities of each field, which originate from the same source. By plugging in (2.7) and (2.8) to equation (2.6) we arrive at:

$$v = \frac{Re\langle E_0^*(t) E_0(t+\tau) \rangle}{\langle |E_0(t)|^2 \rangle} = cos\ (\omega\tau) \tag{2.9}$$

The visibility is equal to the real part of the first order correlation function. In practice, we plot the visibility by calculating:

$$v = \frac{n_4 - n_3}{n_4 + n_3} \tag{2.10}$$

Where n represents the number of photon counts integrated over some time period obtained at one of two detectors, and the numbering is consistent with the intensities. Later in this thesis, we often present results in the form of visibilities. We see above that visibility fringes are of a sinusoidal shape because detection of the light oscillates between the two detectors. The envelope wavefunction capturing the overall behavior of these fringes are used to extract the coherence time. The coherence time is the time it takes for the visibility amplitude to decay to e^{-1} of its initial value. Visibility envelopes are obtained by fitting each fringe to a sine function in order to obtain the maximum and minimum intensity values. Then, the minimum is subtracted from the maximum and this quantity is divided by two. This yields the envelope function that can be fit with an exponential decay to find the coherence time.

2.5 Second order correlation function

The second order correlation function is the intensity analogue of the first order correlation function. While the $g^{(1)}$ function measures amplitude correlation, the $g^{(2)}$ function measures the correlation of intensity fluctuations. It is called "second order" because it depends on the interference of two fields, or detection of two photons, rather than one in the case of the first order correlation function. The second order correlation function is as follows:

$$\begin{aligned} g^{(2)}(\tau) &= \frac{\langle E^*(t)E^*(t+\tau)E(t)E(t+\tau)\rangle}{\langle E^*(t)E(t)\rangle\langle E^*(t+\tau)E(t+\tau)\rangle} \\ &= \frac{\langle I(t)I(t+\tau)\rangle}{\langle I(t)\rangle\langle I(t+\tau)\rangle} = \frac{\langle I(t)I(t+\tau)\rangle}{\langle I(t)\rangle^2} \end{aligned} \tag{2.11}$$

The final form is written based on the assumption that the light source has a constant average intensity so that $I(t) = I(t+\tau)$. Considering the detection of single photons we can write:

$$g^{(2)}(\tau) = \frac{\langle n_{start}(t) n_{stop}(t+\tau)\rangle}{\langle n_{start}(t)\rangle\langle n_{stop}(t+\tau)\rangle} \tag{2.12}$$

This measurement is completed using a Hanbury Brown-Twiss experimental set-up, as seen in Figure 2.4. This consists of a beam splitter and a detector at the end of each of the two paths. Fox (2006) describes it as one detector indicates a "start" signal, and the other a "stop." The number of photons incident on each detector is indicated by $n_{start/stop}$ in equation (2.12). The detectors count the number of incident photons, as well as the time delay, τ, between a photon incident on the start detector and a subsequent photon incident on the stop detector. Essentially, the measurement tells us the likelihood of measuring a photon at the "stop" detector a time τ after measuring one at the "start" detector, by recording how many times this occurs for a given value of τ. The number of photons counted is proportional to the intensity of the collected light. The importance of this measurement is that it can be used to distinguish classical sources of light from those that are anti-bunched, where consecutive photons are emitted with consistent gaps between them and can only be described with a quantum mechanical approach. This is especially relevant in the case of our semiconductor quantum dot sample, because we can verify it is behaving as a single photon source.

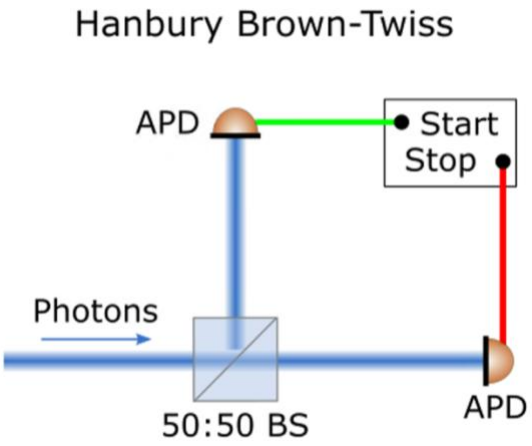

Figure 2.4. Depiction of Hanbury Brown-Twiss experimental set up used for $g^{(2)}(\tau)$ measurements. The counter recording the start and stop photons also measures and records the time between them.

Irrespective of the light source, at large values of τ, $g^{(2)}(\tau) = 1$, since the intensity fluctuations are completely randomized and average out to zero. Additionally, it is known that for bunched light, where photons are emitted in clusters, $g^{(2)}(0) > 1$ and tends towards unity on the order of τ_c. For coherent light, where photon spacing is random, $g^{(2)}(\tau) = 1$ for all values of τ

because the intensity does not fluctuate in time. These results can be derived classically. However, it is also possible to obtain the non-classical result of $g^{(2)}(0) = 0$. This indicates anti-bunching of the light being measured, which is a purely quantum phenomenon [2]. Intuitively this can be understood because the quantum dot can only interact with one photon at a time, so there is a non-zero time in between photon interactions with the QD. As a result, it is highly unlikely that at times close to $\tau = 0$ photons will be detected simultaneously at each detector, resulting in $g^{(2)}(0) = 0$. In practice, we see $0 < g^{(2)}(0) < 0.5$, where the non-zero value at $\tau = 0$ has to do with the time resolution of the detectors being used. However, there have been recent experimental demonstrations showing that anti-bunched photons cannot be observed by collecting only coherently scattered light. There must be both the coherent and incoherent components interfering in order to clearly demonstrate anti-bunching [28].

Although measurement of the second order correlation function is important in demonstrating that anti-bunched photons can be retrieved from a single quantum emitter, in later chapters, this thesis focuses on the analysis and presentation only of the first order correlation function. We are most interested in the coherence time and spin behavior of the electron in our charged quantum dot sample, which is straightforward to extract from the envelope wavefunction of the visibility. We will soon see how phonons contribute to dephasing of the excitonic two level system and how specific light pulses can be used to manipulate the electron spin. First, we will look at how extraneous background laser light plays a role in altering the shape of the visibility envelope and why this must be accounted for.

Chapter 3

Characterization of interferometer

In this chapter, we will examine how the first order correlation function is affected by the proportion of quantum dot signal to background laser light. In order to preface these results, we will first discuss the qualitative shape of the $g^{(1)}$ function obtained when probing neutral and charged quantum dots both with and without the presence of a magnetic field. Then, we will examine how altering the signal to background ratio of interfered light changes the vertical offset present in the fitting function and why this occurs. These results have important implications for the collection and interpretation of visibility measurements. In the experiment presented in this chapter, I aided in performing alignment, and performed most of the data acquisition and data analysis. The setup was designed and the theory in this chapter established by Dr. Andrew Young.

3.1 $g^{(1)}$ of neutral and charged quantum dots

As mentioned briefly in section 2.2, it has been shown experimentally that resonant laser light scattered off a neutral quantum dot retains the first order coherence properties of the excitation laser, rather than taking on optical properties of the QD. This occurs in the coherent scattering regime, where absorption and emission of a photon become a combined, coherent event. It manifests as a visibility spectrum that decays slowly as compared to the decay in visibility produced from performing non-resonant excitation and collecting incoherent events from the neutral quantum dot [24, 25]. From incoherent exciton decay, the upper limit of the coherence time is two times the radiative lifetime of the exciton [24]. Our research group has previously measured the visibility of one of our neutral quantum dot samples both with and without a magnetic field present and we observe this reported effect. This is presented visually in Figure 3.1, where 3.1(a) is without a magnetic field, and 3.1(b) is using a magnetic field of B ~ 72 mT [29]. Both of these plots were obtained using a continuous wave laser power of ~ 0.5 nW. Our interferometer cannot measure times beyond ~ 4 ns and as a result, we cannot resolve at exactly what value of τ the coherence decays. However, for this discussion, the exact value of the

coherence time is not as important as the qualitative observation that the scattered light retains coherence for much longer than it would have if the coherence had been governed by the optical dynamics and timescales intrinsic to the QD.

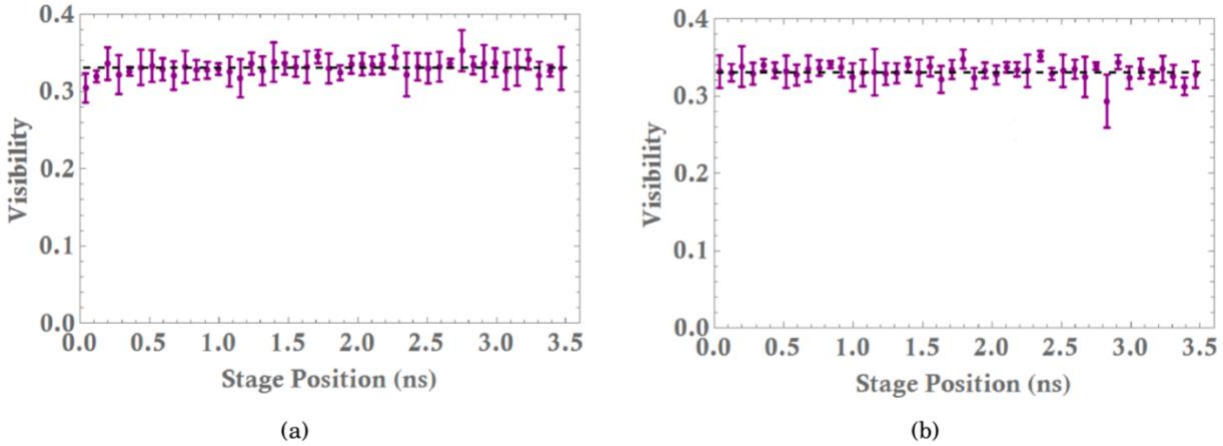

Figure 3.1. Visibility envelopes for a neutral quantum dot measured in **a.** 0 T magnetic field and **b.** ~70 mT magnetic field. Reprinted from "Nuclear spin control and manipulation in self-assembled quantum dots," by J. Hinchliff, *Doctoral dissertation, University of Bristol, Bristol, England* (2018) [29].

However, we observe a radically different behavior of the first order correlation function when probing a charged quantum dot. When there is no applied magnetic field, the visibility decays rapidly, on the order of a few nanoseconds, which provides a measurement of the coherence time of the electron. We can infer from this that collecting visibility measurements of a charged sample yields information about the excess electron [30]. In the presence of a non-zero magnetic field, the visibility envelope demonstrates decaying oscillations. The visibility starts at a maximum value, goes to zero, revives to a value less than the initial visibility, and goes back down to zero. This repeats until the visibility fringes have completely decayed. The envelope decay of these observed oscillations corresponds to the coherence time of the electron in the charged QD sample and may be modified as a result of the applied magnetic field, as compared to the coherence time extracted with zero magnetic field [31]. The data points obtained with no magnetic field can be fit with an exponential decay function, whereas the visibility envelope produced using a non-zero magnetic field can be fit with a modulus cosine function multiplied by an exponential decay term. Plots demonstrating examples of these behaviors are presented in Figure 3.2.

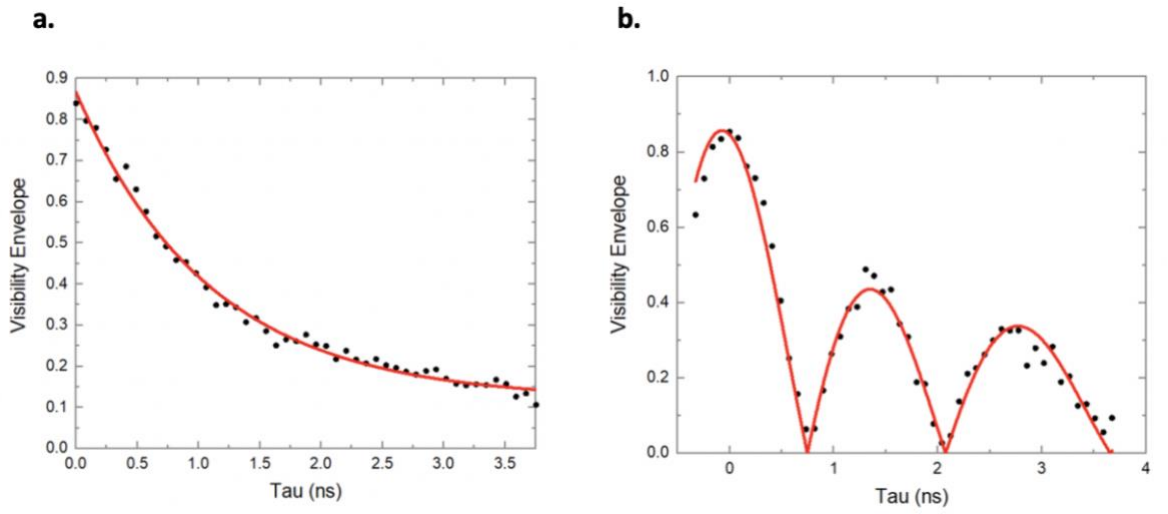

Figure 3.2. Visibility envelopes for a charged quantum dot measured in **a.** 0 T magnetic field probed with a continuous wave laser at P = 1nW and coherence time of 1.09 +/- 0.04 ns and **b.** ~86 mT magnetic field with a continuous wave laser at P = 0.2 nW.

Currently, there is no discussion in the literature describing the observed oscillations in visibility when interfering light scattered from a charged quantum dot. However, our research group is in the process of exploring the meaning and origin of this behavior. The g-factor of the excess electron in a charged quantum dot may have a different value than that of a typical free electron, as governed by factors including the emission energy and shape and strain of the QD. Various experimental approaches can be utilized to reliably measure the g-factor of a charged quantum dot [32]. Researchers in our group have recently shown that the g-factor can also be consistently extracted by plotting the frequency of oscillations as a function of applied magnetic field, as these two variables have a linear relationship, presented in Figure 3.3 [29]. This provides strong evidence indicating that the first order coherence of light scattered from a charged quantum dot is dominated by electron spin and that the oscillations can be mapped onto the state of the electron as it precesses around the magnetic field. At time $\tau = 0$, assume the electron is in the state $|\uparrow\rangle$. When the electron is allowed to precess for a time τ equivalent to a rotation of $\frac{\pi}{2}$ or $\frac{3\pi}{2}$, the electron has rotated to a superposition state $\left(\frac{|\uparrow\rangle \pm |\downarrow\rangle}{\sqrt{2}}\right)$ and this is where we see the collapses in visibility. The light does not have a well-defined phase and therefore demonstrates no interference. The maxima occur at times τ corresponding to rotations of π or 2π, when the electron evolves to the $|\downarrow\rangle$ or $|\uparrow\rangle$ states. This is a working explanation our group has developed, yet it is not explicitly part of my thesis work.

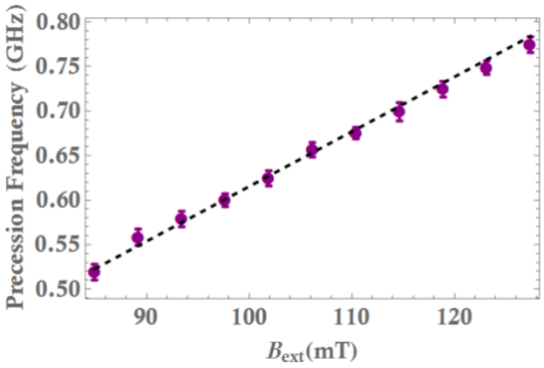

Figure 3.3. Linear relationship of precession frequency of electron spin and applied magnetic (B) field. The charged quantum dot measured here has a calculated g-factor of 0.437. Reprinted from "Nuclear spin control and manipulation in self-assembled quantum dots," by J. Hinchliff, *Doctoral dissertation, University of Bristol, Bristol, England* (2018) [29].

However, the focus of this chapter is not why we see these oscillations, but rather under what conditions. We have collected data demonstrating that by changing the ratio of signal from the charged QD to background light from the continuous wave laser, we change the qualitative shape of the visibility envelope. The data can be modeled with a decaying modulus cosine function plus some constant, where the modulus cosine term captures the oscillations, the overall decay can be used to quantify the coherence time, and the added constant provides a vertical offset due to the background laser light. However, as the ratio decreases, the fundamental shape of the visibility envelope is altered. Upon initial inspection, it appears that the form of the visibility envelope changes from a modulus cosine to a cosine function as the ratio is reduced. We find that at low signal to background ratios, the oscillations are superimposed with a large, coherent background, resulting in an increasing vertical offset.

3.2 $g^{(1)}$ dependence on signal to background ratio

In this experiment, we found that a sufficiently high proportion of interfered light must come from coherent scattering with the sample, as compared to background laser light in order to accurately probe and measure the spin dynamics of the electron in the QD. We probe the charged QD described in section 1.2 within a magnetic field of ~ 86 mT. We plot the visibility envelopes using various ratios of signal to background (S:B) light to examine the effect it has on changing the observed shape of the envelope and explain why this occurs.

The continuous wave (CW) laser, utilized in all of the experiments, is a single frequency tunable Ti:Sapphire laser with a bandwidth less than 10 MHz. We change the amount of measured background laser light by maintaining a constant power of the input, CW laser and rotating the quarter wave plate prior to the sample through small angles. The set-up is depicted in Figure 3.4. The CW laser will have a small component that is horizontally polarized, which allows collection in the cross polarized channel, along with the light that interacts with the sample. By changing the wave plate angle, we can increase this component of horizontal light and thus the background.

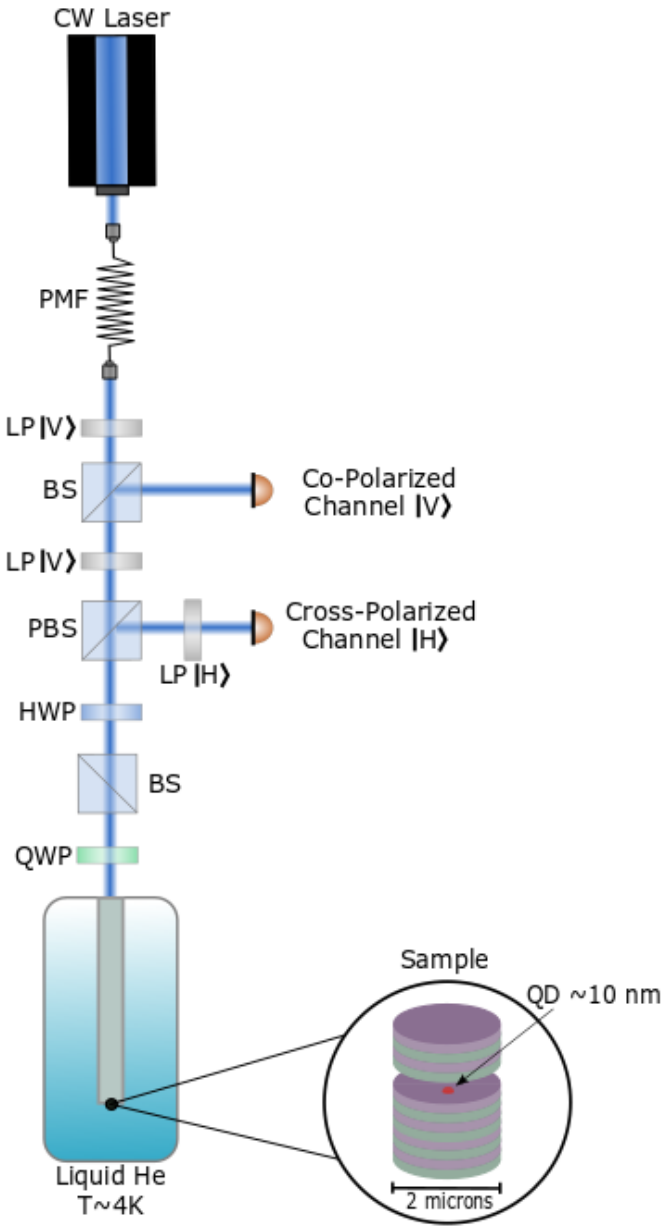

Figure 3.4. Diagram of optics used to control laser light interaction with the sample. H and V indicate polarizations of light (horizontal and vertical, respectively), PMF – polarization maintaining fiber, LP – linear polarizer, BS – beam splitter, PBS – polarizing beam splitter, HWP – half wave plate, and QWP – quarter wave plate.

In order to determine the signal to background ratio, we first perform a wavelength scan where the number of photon counts is measured as a function of wavelength. This is completed after each change in wave plate rotation. The resulting curve is fit with a Gaussian function which is used to determine the amount of counts acquired on and off resonance. Dividing these quantities, we obtain S:B rounded to the nearest half.

We now present the data acquired by maintaining a constant power (~0.2 nW) of the CW laser and rotating the quarter wave plate. The waveplate was rotated in increments of 0.5 or 1 degrees to gradually increase the horizontally polarized component of laser light. These results are presented in Figure 3.5, where the visibility envelopes are presented for different S:B values.

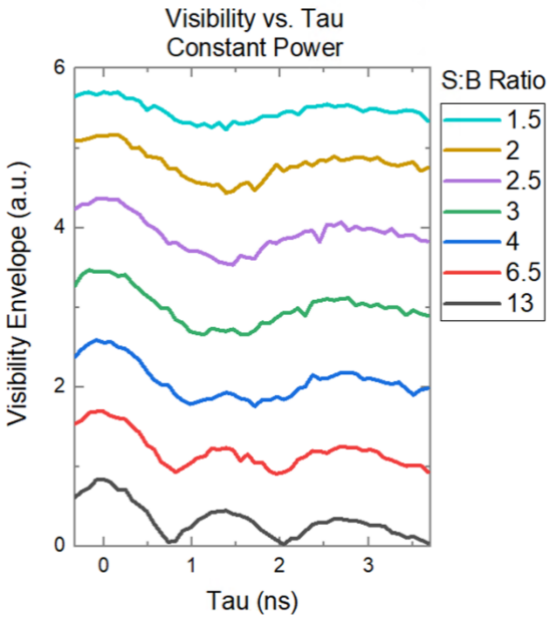

Figure 3.5. Visibility envelopes measured with a constant power and variable wave plate angle, ordered by signal to background ratio. Plots are vertically offset for clarity.

Looking at these plots, we see that there is not a strong demonstration of the second peak until a ratio of ~6.5. However, at this ratio the magnitude of the second peak is still slightly lower than those of the first and third peaks. With a ratio of 13, we observe the expected shape where the decaying oscillations are well-defined, and each subsequent peak has a smaller magnitude. As such, a ratio of ~10 should be achieved to reliably and clearly see the oscillations in the visibility. This is a rough estimate and to find the exact ratio necessary, we must perform more visibility measurements for S:B values between 6.5 and 13.

Fitting each of the measurements individually, we find that the electron precession frequency, or frequency of oscillations, does not vary with the change in background and has a value of 0.35 GHz. Each plot can be accurately modeled using the following function:

$$v = |Acos(2.22 * \tau) * e^{-B*\tau} + C| \quad (3.1)$$

In this formula, A is the signal amplitude, B is the decay time, and C is the vertical offset resulting from the background laser intensity. We find that at low ratios, the visibility envelope appears to take on the shape of a cosine function, which is manifested in the fit as a high value of C, due to the increasingly large amount of background laser light. As the signal to background ratio is increased, the second peak is introduced and increases in magnitude. At the highest ratio measured (13) there is an offset of only 0.06. The next highest ratio (6.5) has an offset of 0.11, but even this is enough to cause a second peak smaller than those adjacent. For the lower ratios, the value of C reliably increases as the ratio declines. The values of C corresponding to each signal to background ratio is presented in Table 3.1, below.

S:B	13	6.5	4	3	2.5	2	1.5
Value of C	0.06	0.11	0.23	0.30	0.37	0.46	0.63

Table 3.1. Table of values demonstrating the value of C, or the vertical offset of the fitting function, corresponding to various signal to background ratios.

Fitted plots demonstrating examples of a low (2.5) and high (13) ratios are presented in Figure 3.6. We find that introducing different amounts of coherent, background laser light causes a vertical offset in the visibility – larger offset with more background and a low signal to background ratio. With this offset, the second peak is not captured at sufficiently low ratios as one can imagine that taking the modulus of an oscillating function would only demonstrate a second peak to the extent that it dips below y = 0. At intermediate signal to background ratios, between ~3-6.5, we would expect to see oscillations where the second peak has a smaller amplitude than the first and third peaks. This is clearly visible in Figure 3.5.

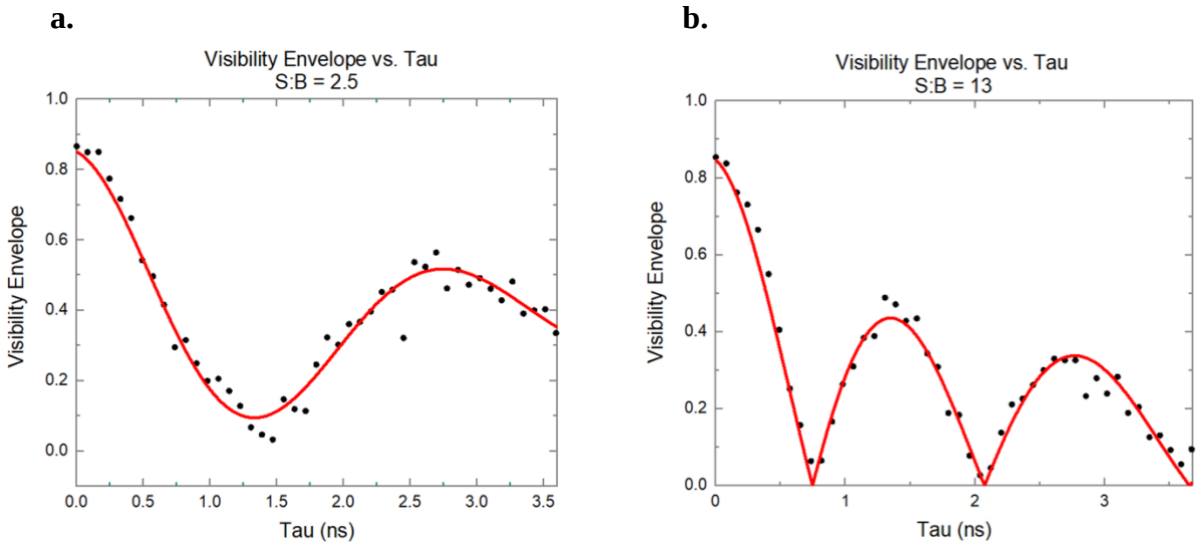

Figure 3.6. Plots exemplifying the qualitative shape of visibility envelopes with **a.** a low (2.5) signal to background ratio and **b.** a high (13) signal to background ratio, both fit with a decaying mod(cos) function.

We performed other measurements in which the signal to background ratio was altered by increasing the power of the CW laser. Although this can be used as another method to demonstrate the effect explained above, we do not present the results here because increasing the power also subjects the two-level system to optically induced dephasing mechanisms that must be taken into account when interpreting the visibility spectrum.

Ultimately, performing this measurement we measure the $g^{(1)}$ function of the quantum dot spin system superimposed with the $g^{(1)}$ function of the CW laser in different proportions. A ratio of roughly 10:1 is necessary to ensure that the data being analyzed is an accurate representation of the QD spin dynamics, and not convoluted by unwanted noise from the laser. This finding was taken into consideration when setting up and collecting data from the experiments detailed in chapters 4 and 5 and is imperative to ensuring correct interpretation of results in future experiments.

It is important to note that it is possible to obtain sufficiently high ratios of quantum dot light compared to background laser light while using a low-quality factor micropillar cavity. These results should be considered and reproduced when conducting experiments utilizing micropillar cavities with much higher quality factors.

Chapter 4

Phonon interactions with charged exciton

In this chapter, we will investigate the phonon sideband of a charged QD in a micropillar cavity. The indistinguishability of photons emitted from QDs is limited by their coupling to vibrational modes of the host cavity. We will briefly examine how phonons affect photon emission and how this is manifested in the spectrum. Additionally, we will compare our results to those previously published in the literature using a neutral QD in a photonic crystal cavity and a charge tunable QD in a Schottky diode device. We will then show results from interferometry measurements of the phonon sideband of our charged QD in the time domain at various excitation powers. In this experiment I assisted in the alignment of optical components and in the data collection itself, although the setup was overall designed by Dr. Andrew Young. I worked with Dr. Dara McCutcheon in order to understand and explain the theory behind the presented results. Finally, I was responsible for processing and analyzing all of the data collected related to this experiment.

4.1 Phonon effect on photon emission

It is important to consider and understand factors from the environment that may cause decoherence of the TLS within a QD, reducing the efficiency and indistinguishability of emitted photons. An important dephasing mechanism is coupling to vibrational modes of the host lattice [33, 34, 35]. Dephasing occurs when the phase relationship between the components of the superposition state of the exciton diminishes, thereby lessening interference [36]. Examining the nature of this specific type of dephasing can aid in determining what filtering or cavity enhancement may be necessary and understanding how this may sacrifice efficiency. The goal of our experiment was to confirm that quantified results using a neutral quantum dot in a photonic crystal cavity and a charge tunable quantum dot in a Schottky diode were reproducible with our charged sample in a micropillar cavity. We aimed to see if it was possible to do these measurements where there is a higher amount of background scattering as compared to a flat sample. This would pave the way for measuring samples in higher Q-factor micropillar cavities.

Observation of the emission spectrum (see Figure 4.1(c)) of the collected light reveals both a sharp peak (called the zero-phonon line) and a broad sideband, whose relative sizes are independent of driving power. The zero-phonon line (ZPL) is comprised of photons with emission energy corresponding to the energy between the ground and excited state of the TLS. It has been demonstrated that broadening of the ZPL due to charge noise in quantum dots can be suppressed so that near transform-limited photons are emitted [37, 38]. The broad sideband arises as a result of longitudinal acoustic (LA) phonon coupling with a fraction of the emitted photons. LA phonons have been shown to be the primary dephasing mechanism in QDs [39]. Instead of photon emission solely into the zero-phonon line, photon emission may be accompanied by the emission or absorption of a phonon. When an exciton is present, the dipole causes lattice deformation as the electron moves to the conduction band and causes a shift in the position of surrounding nuclei. Upon recombination, the lattice relaxes, and the exciton may couple to phonons [35, 40]. This occurrence alters the energy of the emitted photon and results in range of photon energies that comprise the phonon sideband (PSB). At low temperatures, phonon emission is more common than absorption, causing a red-shifted asymmetry in the PSB. Since our experiment is performed at ~4 K, there is minimal extraneous energy present in the system and therefore very few phonons available to be absorbed. The probability of photon emission into the PSB is determined by the expression $1\text{-}B^2$ and the probability of emission into the ZPL is proportional to B^2, where $0 < B < 1$ is the Franck-Condon factor. This quantity is a measure of the overlap of the ground and excited state lattice manifolds, determined by the overlap of their vibrational wavefunctions (see Figure 4.1(b)) [40]. Figure 4.1(a) provides a visual demonstrating how emission of a phonon is accompanied by the emission of a lower energy photon. It should also be noted that even at low temperature and in the coherent scattering regime, it is possible for LA phonon emission to occur [40, 41, 42]. Figure 4.1(d) shows how the probability of emission into the ZPL (B^2, represented by the color spectrum on the right of the figure) varies with temperature and quantum dot size, demonstrating more emissions into the ZPL with lower temperatures and larger QD sizes.

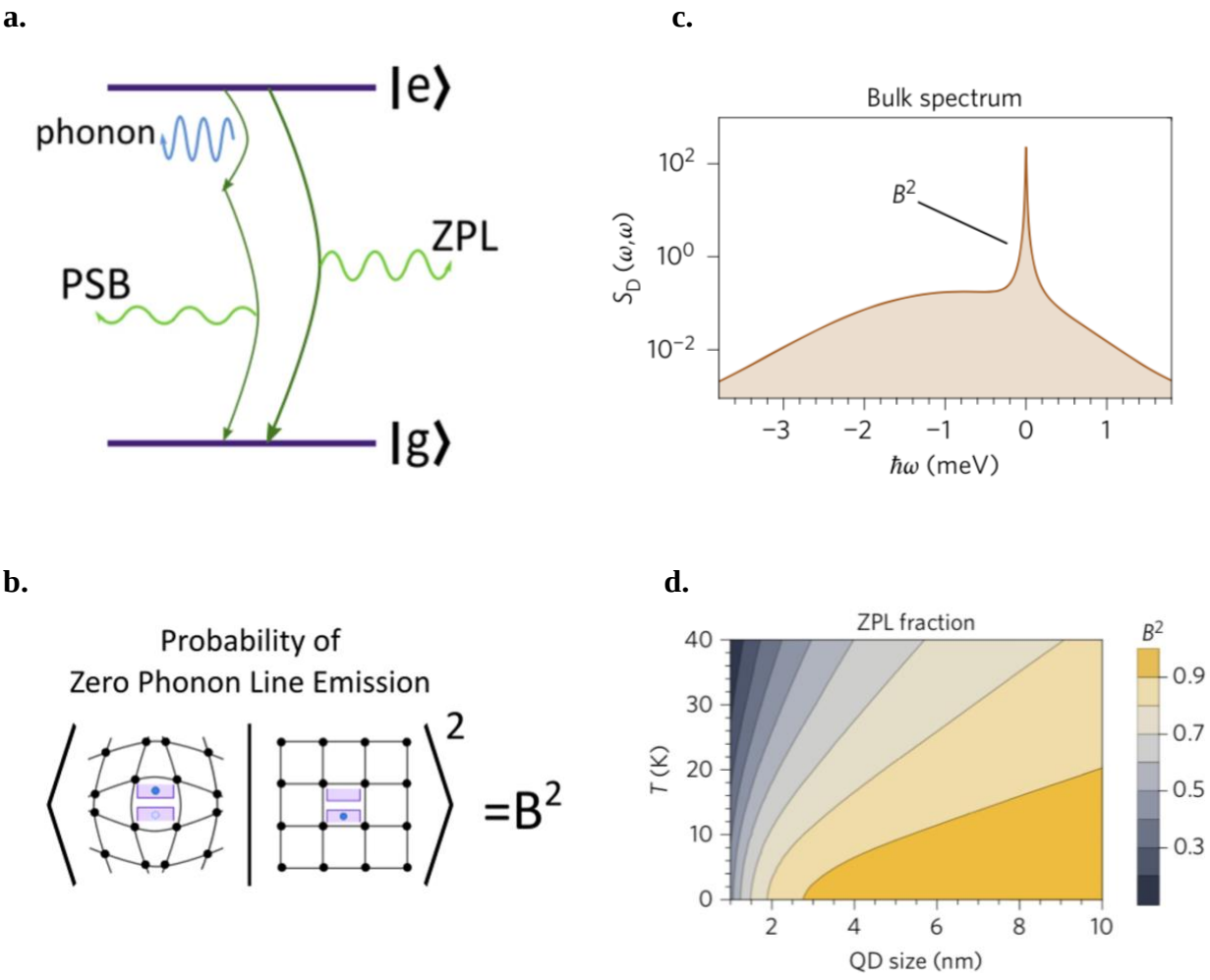

Figure 4.1. a. Diagram of photon emission with and without accompaniment by a phonon. **b.** Calculation of the fraction of emission into the zero-phonon line based on overlap of lattice configurations, where the left lattice represents the excited state and the right lattice represents the ground state. **c.** Emission spectrum displaying narrow peak of ZPL, indicated by B^2 and broad PSB. **d.** Plot demonstrating B^2 dependence on temperature and QD size. B^2 color spectrum is indicated on the right-hand side of the figure. Parts b and d are reprinted from "Phonon scattering inhibits simultaneous near-unity efficiency and indistinguishability in semiconductor single-photon sources," by J. Iles-Smith, D. McCutcheon, A. Nazir, and J. Mørk, *Nature Photonics*, 11(8), pp.521-526. Copyright (2017) by Nature Publishing Group [40].

It is important to acknowledge that our sample is modulation doped with silicon, which could potentially affect the shape and behavior of the lattice, and subsequently phonon coupling. The Hamiltonian governing exciton-phonon interaction dynamics is influenced by features including the mass density of the solid, lattice volume, and the size and shape of electron and

hole wavefunctions [41, 42, 43]. Because the Hamiltonian relies on factors determined by the host lattice, we suspected that the silicon dopants present may slightly modify the resulting phonon coupling. Additionally, the phonon spectral density is determined by the phonon cut-off frequency and deformation potential coupling strength, both of which have standard experimental values in the case of self-assembled GaAs QDs [39, 41, 42]. However, because our sample is modulation doped, unlike the others being used for comparison, we might also expect these values to be slightly different in our case. Finally, one might expect to observe different results between a neutral and charged QD because the extra electron in the trion case would create a different equilibrium state for the ground state lattice as compared to the neutral exciton. This could potentially affect lattice deformation upon scattering or excitation, and subsequent phonon coupling. However, despite these considerations, we don't observe any substantial difference between the quantitative measurements in our sample compared to others, within experimental error.

4.2 Time-domain measurements

In this experiment, we perform measurements of the first order coherence time and percentage visibility of the scattered photons from our negatively charged quantum dot in a micropillar cavity at a range of excitation powers. The percentage visibility reported is the fraction of the interfered light that emits into the PSB, and the remaining fraction is that of the ZPL. The micropillar and QD are described in detail in section 1.2, and this experiment was performed in zero magnetic field.

4.2.1 Experimental method summary

The phonon-mediated interactions occur on a very short timescale, as they correspond to a large spectral width. As such, it is necessary to use the interferometer to perform a fine scan of the visibility around zero time delay so that the coherence of the PSB can be accurately resolved and measured. In order to calibrate the interferometer, a pulsed laser is used in order to determine where $\tau = 0$. The visibility envelope of the pulsed laser is plotted and fit with a Gaussian curve, and the location of the maximum visibility is taken to be $\tau = 0$. To measure the visibility of the PSB, the scattered light from the continuous wave laser is polarization filtered to suppress the

pump, and coupled into our MZ interferometer (described in section 2.3). We scanned the interferometer for delay times τ = -0.7 ps to τ = 4 ps, using different excitation powers up to 3 nW.

Figure 4.2 shows fine (Figure 4.2(a)) and coarse (Figure 4.2(b)) visibility scans of the scattered light at 2 nW. The PSB coherence time was found by fitting an exponential decay function to the visibility envelope for both positive and negative time delays. These are shown in Table 4.1 for all of the powers investigated, for both positive and negative time delays, and plotted in Figure 4.3 for positive time delays only. As can be seen, there is no strong dependence on excitation power of the coherence time, within the limits of the experimental error. It was consistently measured to be on the order of 1 picosecond. Additionally, the measured percent visibility of the PSB was roughly 5-6%, within error, for both negative and positive time delays.

4.2.2 Interpretation of results

Changing the power of the laser changes the ratio of incoherent scattering to coherent scattering events: at higher powers, real excitation becomes prevalent resulting in a greater proportion of incoherent scattering. Far below saturation, the majority of photons are virtually scattered off of the electron spin within the QD, however, we found that around 2 nW, the counts approached saturation and incoherent events became more prevalent.

Regardless of driving strength, we expect LA phonon mediated interactions with photons to be present, as seen when measuring the spectroscopic domain of a charge tunable quantum dot at various Rabi frequencies [42]. We find that the parameters measured in the time domain – visibility and first order coherence time of the PSB, do not strongly depend on excitation conditions. These quantitative findings are consistent with previously published results considering a neutral self-assembled quantum dot in a photonic crystal and a charge tunable quantum dot in a Schottky diode structure, where the PSB was reported to comprise ~6% and ~7-8% of the emission spectra, respectively. [41, 42].

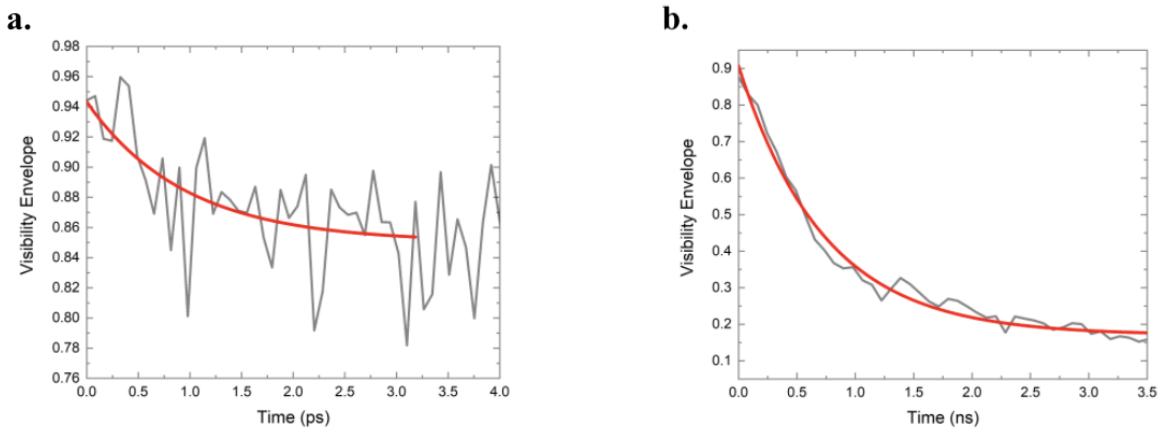

Figure 4.2. Example plots of fine and broad scans of the visibility envelope as a function of time delay, fitted with exponential decay functions. **a.** Fine scan visibility envelope using P=2nW, taken around zero-time delay on the picosecond time scale to resolve the coherence time of the phonon sideband. The decay in visibility for positive time delay yields a coherence time of t = 1.0 +/- 0.5 ps. **b.** Broad scan visibility envelope using P=2nW taken on the nanosecond timescale to resolve the longer coherence of the spin scattered light. The decay in visibility indicates a coherence time of t = 0.7 +/- 0.04 ns.

	Negative Time Delay		Positive Time Delay	
Power	%Visibility	t (ps)	%Visibility	t (ps)
0.2nW	-	-	4.8 +/- 3.1	0.8 +/- 0.5
0.4nW	6.3 +/- 2.2	-1.0 +/- 0.4	5.7 +/- 2.2	0.6 +/- 0.3
2 nW	6.4 +/- 5.1	-1.8 +/- 0.8	6.2 +/- 5.1	1.0 +/- 0.5
3 nW	6.2 +/- 2.4	-0.8 +/- 0.3	5.8 +/- 2.4	1.4 +/- 0.7

Table 4.1. Table of values showing measured percent visibility and coherence time of phonon sidebands measured at various powers. Values for negative and positive time delays are displayed.

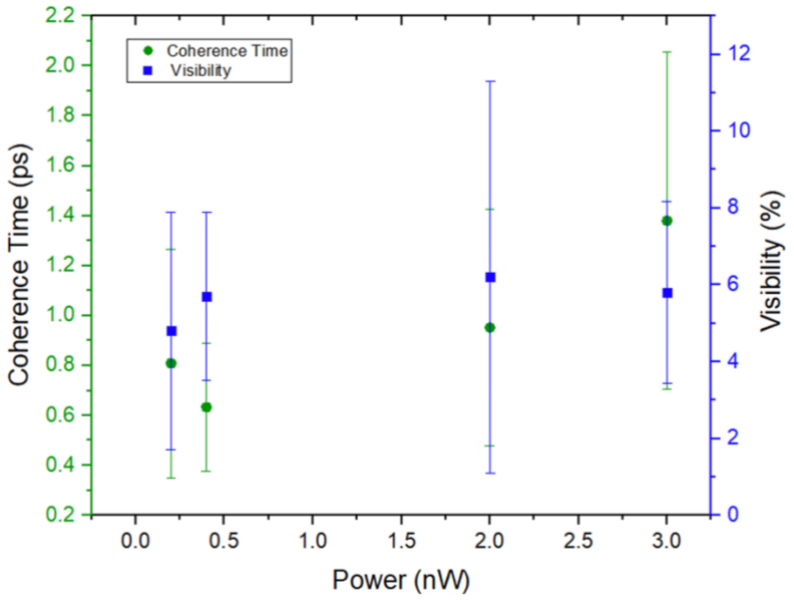

Figure 4.3. Percent visibility and coherence time of the phonon sideband plotted versus power (positive time delay only) with error bars shown. Numerical values, including those for negative time delay, can be found in Table 1.

As a final note, there is a slight asymmetry when comparing the numerical values for coherence time and percent visibility of negative and positive time delays at each respective power. This may be attributed to any slight misalignment in the apparatus or the high noise observed at such short time delays. The values are consistent with one another in terms of order of magnitude and in agreement within the given errors, so the slight asymmetry did not warrant any further investigation. Additionally, we mention in Chapter 3 how increasing the power of the CW laser may negatively affect the signal to background ratio and introduce even more dephasing of the TLS. It is important to recognize that these are preliminary measurements and serve to show that this type of measurement is possible using a quantum dot in a 3D micropillar cavity. Background counts from the laser may be a reason that our visibility spectrums are so noisy and our measurements have substantial errors.

Ultimately, our measurements show that embedding a QD within a micropillar photonic structure does not dramatically change the phononic environment (~5-6%) compared to other work on photonic crystal cavities (~6%) and Schottky charge tunable devices (~7-8%). We have shown that it is possible to extract this information from a micropillar cavity, setting a precedence for future experiments utilizing higher Q-factor micropillars.

Chapter 5

Coherent control of a solid spin state

In this chapter, we will investigate the first order coherence function of an electron spin within a charged QD, probed with a continuous wave laser and simultaneously driven with a detuned, pulsed laser. The ultimate goal is to demonstrate control over the shape of the output photon wave packet by altering the polarization and power of the pulses. We briefly introduce the concept of coherent control and describe the experimental and optical set up used to carry out our experiment. Then, we discuss why we expect to see differing results when using linear versus circular polarization of pulses. Finally, we present results demonstrating how the first order coherence evolves as a function of pulse power and explain the implications. For this experiment, I took on most of the responsibility in the laboratory in terms of adjusting optical components, adjusting laser power between measurements, and running measurements. I have been working in collaboration with other members of this research group (Dr. Andrew Young and Joseph Lennon) in order to develop a working understanding of this experimental results. Alongside these individuals, I also contributed greatly to the data analysis in terms of calculating and plotting the visibilities presented later in the chapter.

5.1 Coherent control of an electron spin

Single electron spins in charged semiconductor quantum dots are promising candidates for realizing quantum computing and information processing protocols. Coherent manipulation of the electron spin via ultrafast optical laser pulses have been proposed to control the electron spin within the relatively substantial coherence times of these systems, which can reach up to ~ 1 μs [44, 45, 46, 47, 48]. Utilizing optical pulses on the picosecond or femtosecond time scale allows rotations of the spin to be orders of magnitude faster than the Larmor precession period.

The aim of coherent control is to deterministically transform an initial state to a final, target state via an externally applied optical field. This can be used to realize single qubit gates and optically access all points on the Bloch sphere in a controlled fashion, which requires manipulation of both the angle and axis of rotation [22]. It is necessary to apply a magnetic field

in the Voigt geometry (x basis, by our convention) as optical selection rules dictate that the electron spin eigenstates along the magnetic field can be coupled to one another via the excited, trion state acting as an intermediary [44, 46, 47, 49, 50]. This is depicted in Figure 5.1 and we use this four-level structure consisting of two lambda systems to describe our experiment, with further explanation and details provided in subsequent sections. By detuning the pulsed laser off resonance by an amount Δ, this prevents population in the excited state and allows for coherent rotation of the electron spin, in a manner similar to Stimulated Raman adiabatic passage (STIRAP), commonly used in atomic and molecular physics [51]. Traditionally, STIRAP utilizes a lambda system in order to transfer population from one quantum state to another, via a third state that is optically accessible by both. However, STIRAP uses the consecutive application of two separate, coherent fields that independently couple the initial and final states to the transitional state in order to transfer the population, whereas we apply a singular, detuned pulse to couple the two ground states and stimulate rotation of the electron [52]. We will show later that we can only successfully rotate the electron spin with application of circularly polarized pulses, which can be understood intuitively as it drives both the vertical and cross transitions that make up the lambda system, simultaneously. This rotates the spin towards the up or down state in the x basis, and the degree to which it rotates depends on applied pulse power. Additionally, as a result of the Zeeman splitting resulting from the applied magnetic field, this configuration also lends itself to spin initialization via optical pumping [50, 53]. Take, for example, the lambda system composed of the two transitions $|\uparrow_x\rangle \leftrightarrow |\uparrow\downarrow\Uparrow\rangle$ and $|\downarrow_x\rangle \leftrightarrow |\uparrow\downarrow\Uparrow\rangle$. Because these two transitions have different energies, it is possible to drive only the $|\uparrow_x\rangle \rightarrow |\uparrow\downarrow\Uparrow\rangle$ transition on resonance, which will then decay to $|\uparrow_x\rangle$ or $|\downarrow_x\rangle$ with an equal probability. The electron spin can be initialized to $|\downarrow_x\rangle$ by repeating this process, since that transition is undisturbed.

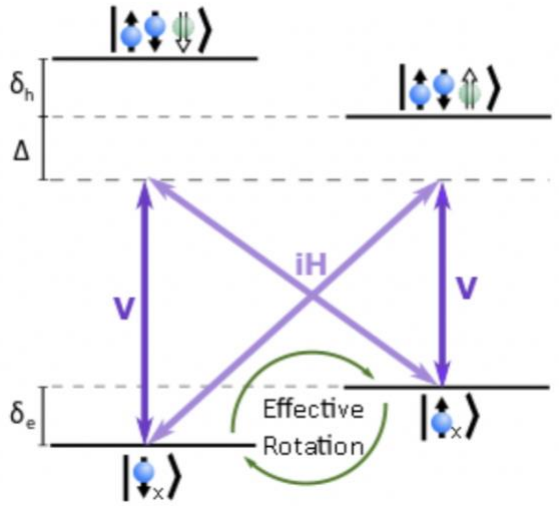

Figure 5.1. Optical transitions of effective four-level system under an applied Voigt magnetic field used in our experiment. Two lambda systems can be seen and the arrows are labelled with the polarization of light that causes the corresponding transition. δ_e represents the energy splitting between the electron ground states, δ_h between the two trion states, and Δ represents the detuning of the pulsed laser (not to scale).

A thorough set of experiments reported by Press et al. (2008) demonstrates full coherent optical control of an electron spin through the measurement of Rabi oscillations. In this context, Rabi oscillations refer to oscillations, or rotations, of the spin vector of the electron between the up and down states in the basis of the magnetic field as a function of pulse area of the applied pulse. Pulse area is proportional to the integral of the electric field amplitude over all times. A pulse area that is an odd multiple of π will rotate the spin by 180° to the opposite spin state, and an even multiple will rotate the spin completely around the Bloch sphere, returning it to its original spin state [2, 54]. The experiment also demonstrated Ramsey interference fringes where two $\pi/2$ pulses were applied, separated by a variable time delay during which the electron spin vector was free to precess about the magnetic field and its position was measured after the second rotation pulse [50]. We draw inspiration from these findings in order to see if it is possible to coherently manipulate and read out the electron spin state via first order coherence measurements. Although we do not initialize our spin state, we find that when using circularly polarized pulses we can successfully rotate the electron spin so that it is in a steady state, aligned along the magnetic field.

5.2 Optical set up/configuration

The optical configuration used in this experiment involves three main components. The first being a series of beam splitters, linear polarizers, half waveplates, and quarter waveplates used to control the polarization of the input laser fields as well as the collection of the light, which is depicted in Figure 5.2. We use a continuous wave laser applied on resonance to probe the spin state of the electron and a detuned, red-shifted pulsed laser to rotate the spin state. The pulsed laser is detuned by an amount Δ. In practice, this detuning is roughly 3-5 nm. The pulse duration is ~2 ps and the pulses are separated by a time of ~13 ns, so they are unsynchronized with the spin precession.

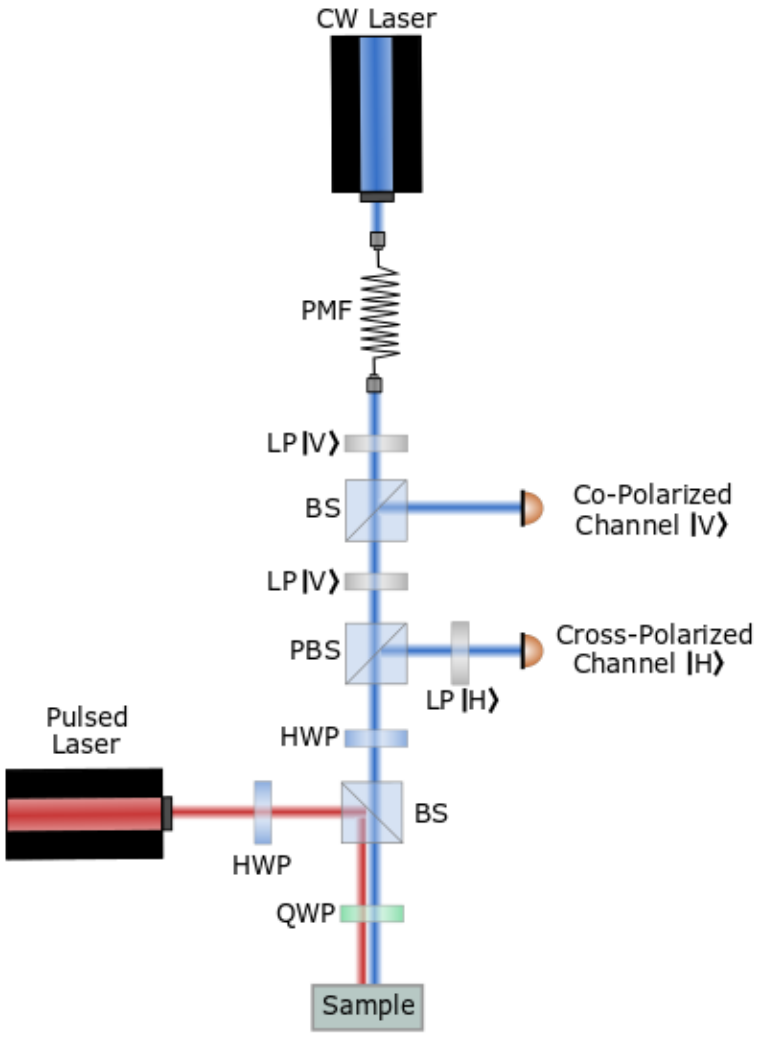

Figure 5.2. Diagram of first portion of experimental set up showing the pulsed and CW laser interaction with the sample and subsequent collection.

A small magnetic field of 86 mT is applied to the sample in the Voigt geometry. The Voigt field is along the x axis, perpendicular to the optical axis (z axis). As we apply this field, the eigenstates of the spin become aligned with the magnetic field. Additionally, we generate two lambda systems as the optical transitions from ground state to either excited, trion state can be optically accessed via vertical or cross linear transitions, as pictured in Figure 5.1. The electron states are depicted with one single arrow, and the trion states are depicted as two electrons with opposite spins, forming a spin singlet, along with a double arrow representing the hole. As aforementioned, this allows coupling of the two ground states, depending on the applied pulses. This will be explained further in the next section. Vertical transitions are achieved using vertically polarized light and cross transitions with horizontally polarized light that is out of phase with the vertical transitions by $\pi/2$. There is an energy difference between the two trion states and the two ground states due to Zeeman splitting, resulting in four transitions, each corresponding to a different energy. The Zeeman splitting energies are denoted by δ_e and δ_h between the electron and hole states, respectively. However, because our magnetic field is small in magnitude, it is not possible to resolve these energy differences spectrally. Additionally, the frequency detuning of the pulsed laser, Δ, is much larger than the Rabi frequencies of the horizontally and vertically polarized light. This acts to mitigate real excitation.

The second main component of this experimental set up consists of a spectrometer (Figure 5.3). The light from the cross polarized channel is directed to the spectrometer via a polarization maintaining fiber. The light is spatially separated using a grating and spatially filtered upon exit. This is to ensure that any extraneous light from the pulsed laser is removed. Finally, the light from the spectrometer is guided to a Mach Zehnder interferometer where the first order coherence is measured (Figure 5.3). We collect this data using both linearly and circularly polarized pulses at various powers in order to elucidate how these factors influence the first order coherence with the goal of demonstrating coherent control of the electron spin.

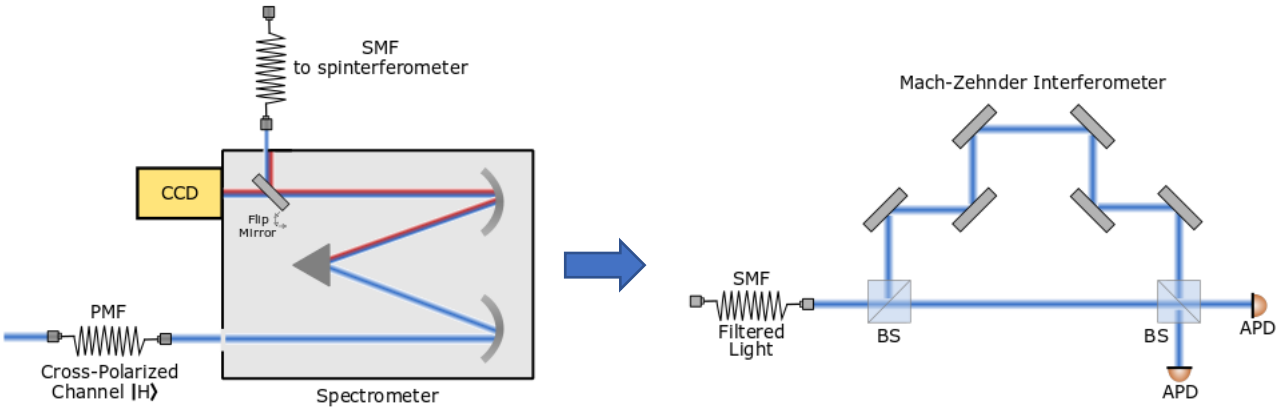

Figure 5.3. Diagram of the spectrometer (left) and Mach-Zehnder interferometer (right) used to filter the light from the cross polarized channel and subsequently measure the first order coherence. When the mirror in the spectrometer is flipped, the signal goes to the CCD where the spectrum of the light can be measured. SMF – single mode fiber, CCD – charge-coupled device, APD – avalanche photodiode.

5.3 Effects of linearly and circularly polarized pulses

As stated in the previous section, we perform this experiment using both linearly and circularly polarized pulses (LP, CP) to compare their effects on the electron's first order coherence. We are able to predict the expected results by looking at the Hamiltonian of the effective two-level system in each case. The following equations and derivations are based off of the work from Press et al. (2008) [50]. We begin our analysis by first considering the case of CP pulses, followed by LP pulses, and finally show experimental results as a function of pulse power.

5.3.1 Circularly Polarized Pulses

The Hamiltonian describing our complete four-level system depicted in Figure 5.1 in the rotating frame of the pulsed laser is given by:

$$\frac{H(t)}{\hbar} = -\delta_e|\uparrow\rangle\langle\uparrow| + \Delta|\Downarrow\rangle\langle\Downarrow| + (\Delta + \delta_h)|\Uparrow\rangle\langle\Uparrow|$$

$$+\frac{1}{2}\Omega_V F(t)(|\Downarrow\rangle\langle\downarrow| + |\Uparrow\rangle\langle\uparrow| + |\uparrow\rangle\langle\Uparrow| + |\downarrow\rangle\langle\Downarrow|) \quad (5.1)$$

$$+\frac{i}{2}\Omega_H F(t)(|\Downarrow\rangle\langle\uparrow| - |\Uparrow\rangle\langle\downarrow| - |\uparrow\rangle\langle\Downarrow| + |\downarrow\rangle\langle\Uparrow|)$$

Here, Ω_H and Ω_V are the Rabi frequencies of the horizontal and vertical components of the pulsed laser light, proportional to the electric field amplitudes of the rotation pulse components and dipole strength, and F(t) is the normalized envelope function of the pulse. The ground state electrons are denoted with single arrows and the excited states are denoted with double arrows, representing a hole, where the direction indicates whether they are spin up or spin down. Although the excited, trion states are composed of a hole and two electrons in a spin singlet configuration, we represent the excited states as $|\Uparrow\rangle$ or $|\Downarrow\rangle$, where the electrons are omitted for convenience of notation. We solve the time independent Schrödinger equation using the generalized four state ket vector:

$$|\Psi\rangle = c_0|\uparrow\rangle + c_1|\downarrow\rangle + c_2|\Downarrow\rangle + c_3|\Uparrow\rangle \tag{5.2}$$

We use $\frac{d}{dt}\langle\Downarrow|\Psi\rangle = \frac{d}{dt}\langle\Uparrow|\Psi\rangle = 0$ because we assume there is negligible excited state population due to the large amount of pulsed laser detuning and this is fixed over time. As a result, we obtain the following Hamiltonian describing the effective two-level system in matrix format:

$$\frac{H(t)}{\hbar} = \begin{pmatrix} -\delta_e - \frac{1}{4\Delta}\Omega_H^2 F^2(t) - \frac{1}{4(\Delta+\delta_h)}\Omega_V^2 F^2(t) & \frac{i}{2}\Omega_{eff} \\ \frac{-i}{2}\Omega_{eff} & -\frac{1}{4\Delta}\Omega_V^2 F^2(t) - \frac{1}{4(\Delta+\delta_h)}\Omega_H^2 F^2(t) \end{pmatrix} \tag{5.3}$$

The term Ω_{eff} in the off diagonal terms is $\approx \frac{\Omega_V \Omega_H}{\Delta}$ and this approximation is made assuming that the detuning is much greater than the Zeeman splitting of the holes, and using the approximation F(t) = 1 while the pulse is on. This term is the effective Rabi frequency perpendicular to our eigenbasis that is along the x axis. Because we see this term in the off-diagonal elements, we expect coupling between the two states $|\uparrow_x\rangle$ and $|\downarrow_x\rangle$. These off-diagonal elements create a mixture of the two, whose proportion is dependent on the power of the pulse. Intuitively, circularly polarized pulses are an equal combination of horizontally and vertically polarized light, where the two components are separated by a phase shift of π/2. As a result, we would expect rotation between the two ground states because CP pulses cause the vertical and cross transitions to occur, simultaneously.

The δ_e component in one of the diagonal terms is responsible for rotation of the spin vector around the magnetic field. This indicates that a vector with a component perpendicular to

the x axis will precess, and when aligned with the magnetic field we will not observe oscillations in the visibility.

5.3.2 Linearly polarized pulses

To reflect our analysis in the case of LP pulses, our four-level system Hamiltonian becomes:

$$\begin{aligned}\frac{H(t)}{\hbar} &= -\delta_e|\uparrow\rangle\langle\uparrow| + \Delta|\Downarrow\rangle\langle\Downarrow| + (\Delta+\delta_h)|\Uparrow\rangle\langle\Uparrow| \\ &+\tfrac{1}{2}\Omega_V F(t)(|\Downarrow\rangle\langle\downarrow| + |\Uparrow\rangle\langle\uparrow| + |\uparrow\rangle\langle\Uparrow| + |\downarrow\rangle\langle\Downarrow|) \\ &+\frac{1}{2}\Omega_H F(t)(|\Downarrow\rangle\langle\uparrow| - |\Uparrow\rangle\langle\downarrow| + |\uparrow\rangle\langle\Downarrow| - |\downarrow\rangle\langle\Uparrow|)\end{aligned} \tag{5.4}$$

Using the same approach and assumptions as in the previous section, we obtain an effective two-level system Hamiltonian with zero off-diagonal terms:

$$\frac{H(t)}{\hbar} = \begin{pmatrix} -\delta_e - \frac{1}{4\Delta}\Omega_H^2 F^2(t) - \frac{1}{4(\Delta+\delta_h)}\Omega_V^2 F^2(t) & 0 \\ 0 & -\frac{1}{4\Delta}\Omega_V^2 F^2(t) - \frac{1}{4(\Delta+\delta_h)}\Omega_H^2 F^2(t) \end{pmatrix} \tag{5.5}$$

Contrary to using CP pulses, in the linear case we do not expect to see coupling between the two eigenstates $|\uparrow_x\rangle$ and $|\downarrow_x\rangle$, due to the lack of off-diagonal matrix elements. We still expect to see oscillations if the state has any non-zero component orthogonal to the x-axis due to the diagonal terms and the diagonal matrix elements are responsible for slight rotations around the x axis. However, if the system were to be initialized in one of the eigenstates, this Hamiltonian dictates that it would remain in that steady state, even after interaction with pulses.

5.3.3 Power dependence

We investigate the power dependence of the first order coherence of the electron spin under two different pulsed laser polarization conditions. We present findings in the form of visibilities and visibility envelopes to reveal, qualitatively, changes in behavior with increasing power. Figure 5.4 depicts our results for CP pulses, and Figure 5.5 our results for LP pulses.

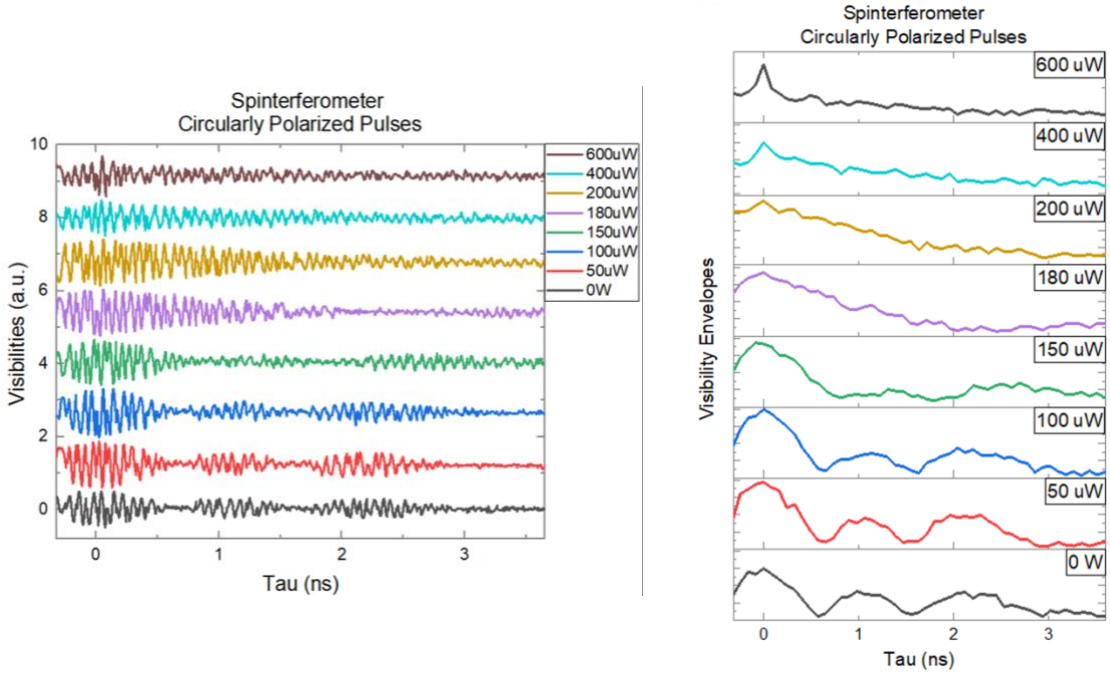

Figure 5.4. Visibilities (left) and visibility envelopes (right) plotted as a function of time delay for various powers of circularly polarized pulses. Visibility plots are vertically offset for clarity. Visibility envelopes are stacked and the y axis ranges from 0 to 0.70 for each envelope.

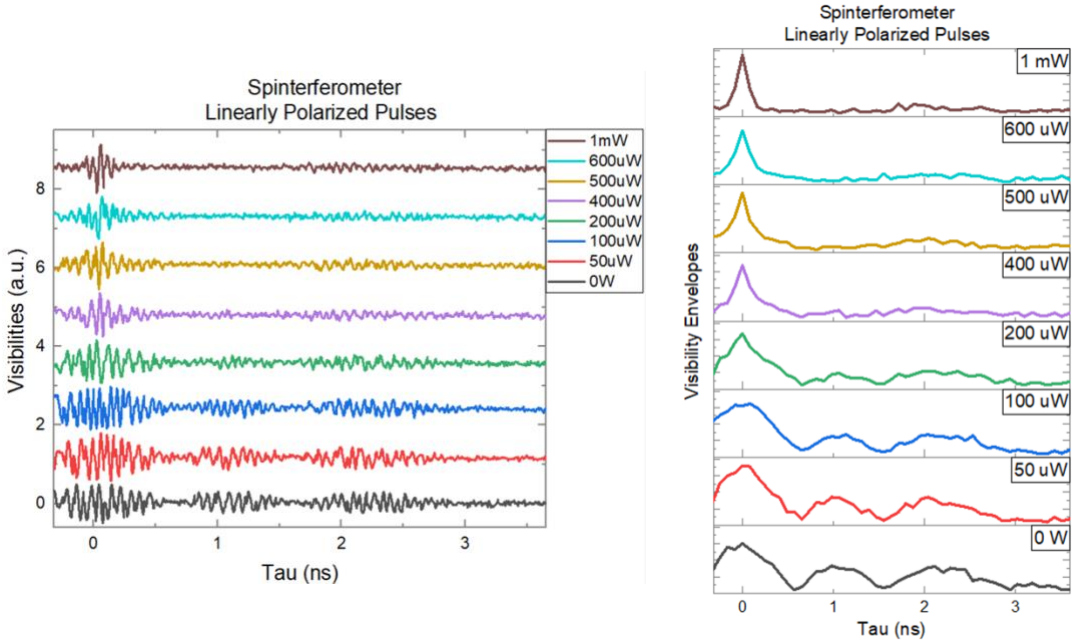

Figure 5.5. Visibilities (left) and visibility envelopes (right) plotted as a function of time delay for various powers of linearly polarized pulses. Visibility plots are vertically offset for clarity. Visibility envelopes are stacked and the y axis ranges from 0 to 0.70 for each envelope.

As seen in the evolution of the visibility as pulse power is increased, CP pulses have a different effect on the spin state than LP pulses, as we would expect based on the difference in effective Hamiltonians presented previously. It appears that in the linear case, we see oscillations in the visibility, independent of power. However, the overall visibility envelopes seem to reduce in amplitude as pulse power is increased. One likely explanation is a change in the resonance frequency of the quantum dot due to the optical Stark effect, resulting in the emission and collection of fewer coherent photons. As the power of the pulsed laser increases, this introduces additional charge traps around the quantum dot, which then alters the electric field the QD is exposed to, and subsequently changes the resonant frequency. This has been previously observed in coherent control experiments using an InGaAs QD in a nanobeam waveguide [55].

Another thing to note is that a Lorentizan shaped peak proliferates and becomes more defined at $\tau = 0$ ns for higher powers in both the CP and LP cases. We have confirmed that this is due to the pulsed laser. Each pulse is ~2 ps in duration and therefore has a broad bandwidth. Once it is filtered via the grating spectrometer, the bandwidth is reduced, effectively lengthening the pulse in time. This manifests itself as a peak with a decay of ~100 ps, which has been corroborated by previous experimental results utilizing these instruments. Lastly, for both cases,

when oscillations are present, the second peak has a lower amplitude than the first and third peaks. We previously demonstrated in chapter 3 that this is indicative of a non-trivial amount of interfering background laser light from the continuous wave laser. In future experiments, we will scan over the resonance frequency of the quantum dot each time the pulsed laser power is increased and adjust the continuous wave laser accordingly, as well as aim to achieve a signal to background ratio of at least 10 in order to prevent the potential issues mentioned.

5.4 Discussion

Overall, we see a fundamental difference between the behavior of the system when perturbed with linear versus circular pulses. In the LP case, we see oscillations of the first order coherence with a consistent precession frequency at each power measured. However, in the CP case, we see a fundamental change in the shape of the visibility envelope as pulse power is increased. Although this is not coherent control in the traditional sense that we can extract specific information about the spin state and generate well-defined rotations about two arbitrary axes, we can change the coherent evolution of the electron spin with pulse power, as evidenced by the change in the first order coherence function. The circularly polarized pulses act to generate superpositions of the eigenstates $|\uparrow_x\rangle$ and $|\downarrow_x\rangle$, whose proportions depend on the power of the pulse. Previous experiments with QD ensembles have demonstrated that it is possible to prepare the spin in a steady state along the magnetic field using unsynchronized pulses [56]. We see evidence of this using our single quantum dot when pulsed at a power of 200 uW, as we no longer see oscillations in the visibility. In chapter 3 we saw that oscillations in the first order coherence function are a direct result of Larmor precession of the electron in the magnetic field. If the spin is prepared along the magnetic field, it no longer has a component orthogonal to the field which is capable of precessing, so we see an exponential decay rather than decaying oscillations. It appears that once the spin is prepared in a steady state of the field it remains there at higher powers, as we do not see oscillations again at 400 nW nor 600 nW.

Initially, it was hypothesized that the change in precession frequency seen at intermediate powers (50-180 uW) was the result of nuclear frequency focusing, in which the nuclear spins surrounding the quantum dot provide an effective magnetic field, or Overhauser field, opposite to the applied magnetic field, slowing the Larmor precession. This occurrence could have been due to the control pulses, a phenomenon previously measured in an ensemble of quantum dots

[57]. However, we verified that there is no revival of oscillations at increased time delays, which was measured by introducing an optical fiber in one path to effectively lengthen one arm of the interferometer. Instead the change in frequency of the oscillations may be explained if the pulses are not perfectly circular, as this would cause an effective change in the Zeeman splitting, and thus the precession frequency [58]. Ultimately, these intermediate powers (50-180 uW) are thought to be transition regions in which the component aligned along the magnetic field is increasing with increasing power. The pulses attempt to prepare the spin in a steady state, however there is still some residual population precessing in the magnetic field resulting in the observed oscillations, as this is a time-averaged measurement.

Currently, we examine the time-averaged behavior of the spin state, rather than the time resolved spin vector and thus, we cannot completely demonstrate control over the entire Bloch sphere. However, we do find that it is possible to prepare the spin in an eigenstate aligned with the magnetic field given the use of circularly polarized laser pulses with sufficient power. We have also demonstrated that linearly polarized pulses do not have this same effect. This measurement method cannot be used to perform single gates on the electron spin however, it is demonstrative of the ability to change the visibility output by modifying the photon wave packet through manipulation of the electron spin state. Here, we have presented our preliminary findings and understanding of coherent control, which we will develop further moving forward. Future experiments will aim to time resolve these measurements and initialize the spin via optical pumping, as well as improve the signal to noise ratio and ensure the continuous wave laser is on resonance with the dot before each individual measurement.

Chapter 6

Conclusion

This chapter aims to summarize the findings presented in each of the preceding experimental chapters, as well as discuss implications and future directions for research. Throughout this thesis, we discussed the measurement of the first order correlation function of a charged In(Ga)As quantum dot within a micropillar cavity in order to investigate decoherence mechanisms and spin control so that these solid state emitters may be used in future quantum information processing applications including quantum memory and quantum computation.

In Chapter 3, we examined how the qualitative shape of the first order correlation function is altered as the amount of background laser light compared to light that has deterministically interacted with the sample changes. We found that a higher proportion of background laser light generates a vertical offset in the visibility, resulting in an apparent distortion of the expected results. Consequently, there is a minimum signal to background ratio that one must achieve so that the visibility measurements accurately reflect the spin dynamics of the electron, and this should be taken into consideration when performing future measurements to prevent misinterpretation of results. Additionally, this experiment provided proof of principle demonstrating that sufficiently high amounts of light from a quantum dot can be obtained when imbedded in a low quality micropillar cavity. The next step would be to extend this to quantum dots in higher quality factor micropillar cavities.

Chapter 4 pertains to the characterization and quantization of the phonon sideband of our charged quantum dot sample. The coupling of the exciton to vibrational modes of the host lattice can have a negative impact on the efficiency and indistinguishability of the quantum dot as a single photon source. We measured the coherence time and the percent visibility of the phonon sideband at different powers within the weak excitation regime. Ultimately, we demonstrated that our results were in agreement with previously published results using a neutral quantum dot in a photonic crystal cavity and a charged quantum dot in a Schottky diode. This experimental demonstration was significant in that it showed that the phonon sideband maintained the same characteristics irrespective of quantum dot charge and cavity structure used. It is important to

understand the prevalence of the phonon sideband present as this must be suppressed when aiming to improve the indistinguishability of the photons emitted from a quantum dot.

Finally, in Chapter 5 we discussed preliminary experimental results in which the spin of the electron within our quantum dot was coherently manipulated via the application of ultrafast, detuned, unsynchronized pulses with different polarizations. We found that circularly polarized control pulses can be utilized in order to change the shape of the output photon wave packet. We saw an evolution in the visibility spectrum with increasing power from oscillatory behavior to a monochromatic decay, implying that the electron spin was prepared in a steady state along the axis of the applied magnetic field. The coherent control of an electron spin has important implications in terms of being able to perform single-qubit gates within the coherence time of the spin. Future work should be undertaken to initialize and time-resolve these measurements, improve the signal to noise ratio, ensure that the quantum dot is on resonance after each subsequent measurement, and collect data for smaller power increments.

Overall, this research contributes to our knowledge of the dephasing mechanisms and spin dynamics of charged quantum dots within photonic cavities and motivates future work to be done to improve and better understand these systems so that they may be used as a platform quantum computation and information.

Bibliography

[1] Einevoll, G. T. (1992). Confinement of excitons in quantum dots. *Physical Review B, 45*(7), 3410.

[2] Fox, M. (2006). *Quantum optics: an introduction* (Vol. 15). OUP Oxford.

[3] Semiconductors on NSM Archive from the Ioffe Institute. (n.d.). Retrieved August, 2020, from http://www.ioffe.ru/SVA/NSM/Semicond

[4] Oulton, R. (2019). *Quantum Dots for Quantum Technologies: Solid-state atom-cavity QED and beyond: Lecture 1*. Personal Collection of R. Oulton, Centre for Quantum Photonics at University of Bristol, Bristol, England.

[5] Loss, D., & DiVincenzo, D. P. (1998). Quantum computation with quantum dots. *Physical Review A, 57*(1), 120.

[6] Ladd, T. D., Jelezko, F., Laflamme, R., Nakamura, Y., Monroe, C., & O'Brien, J. L. (2010). Quantum computers. *Nature, 464*(7285), 45-53

[7] Calarco, T., Datta, A., Fedichev, P., Pazy, E., & Zoller, P. (2003). Spin-based all-optical quantum computation with quantum dots: Understanding and suppressing decoherence. *Physical Review A, 68*(1), 012310.

[8] Nielsen, M. A., & Chuang, I. (2002). Quantum computation and quantum information.

[9] Buckley, S., Rivoire, K., & Vučković, J. (2012). Engineered quantum dot single-photon sources. *Reports on Progress in Physics, 75*(12), 126503.

[10] Senellart, P., Solomon, G., & White, A. (2017). High-performance semiconductor quantum-dot single-photon sources. *Nature nanotechnology, 12*(11), 1026.

[11] Lindner, N. H., & Rudolph, T. (2009). Proposal for pulsed on-demand sources of photonic cluster state strings. *Physical review letters*, *103*(11), 113602.

[12] Goldstein, L., Glas, F., Marzin, J. Y., Charasse, M. N., & Le Roux, G. (1985). Growth by molecular beam epitaxy and characterization of InAs/GaAs strained-layer superlattices. *Applied Physics Letters*, *47*(10), 1099-1101.

[13] Tartakovskii, A. (Ed.). (2012). *Quantum dots: optics, electron transport and future applications*. Cambridge University Press.

[14] Mar, J. D., Xu, X. L., Baumberg, J. J., Brossard, F. S. F., Irvine, A. C., Stanley, C., & Williams, D. A. (2011). Bias-controlled single-electron charging of a self-assembled quantum dot in a two-dimensional-electron-gas-based n− i-Schottky diode. *Physical Review B*, *83*(7), 075306.

[15] Reitzenstein, S., & Forchel, A. (2010). Quantum dot micropillars. *Journal of Physics D: Applied Physics*, *43*(3), 033001.

[16] Reitzenstein, S., & Forchel, A. (2010). Quantum dot micropillars. *Journal of Physics D: Applied Physics*, *43*(3), 033001.

[17] Solomon, G. S., Pelton, M., & Yamamoto, Y. (2001). Single-mode spontaneous emission from a single quantum dot in a three-dimensional microcavity. *Physical Review Letters*, *86*(17), 3903.

[18] O'brien, J. L., Furusawa, A., & Vučković, J. (2009). Photonic quantum technologies. *Nature Photonics*, *3*(12), 687-695.

[19] Moreau, E., Robert, I., Gérard, J. M., Abram, I., Manin, L., & Thierry-Mieg, V. (2001). Single-mode solid-state single photon source based on isolated quantum dots in pillar microcavities. *Applied Physics Letters*, *79*(18), 2865-2867.

[20] Pelton, M., Santori, C., Vucković, J., Zhang, B., Solomon, G. S., Plant, J., & Yamamoto, Y. (2002). Efficient source of single photons: a single quantum dot in a micropost microcavity. *Physical review letters*, *89*(23), 233602.

[21] Bayer, M., Ortner, G., Stern, O., Kuther, A., Gorbunov, A. A., Forchel, A., ... & Walck, S. N. (2002). Fine structure of neutral and charged excitons in self-assembled In (Ga) As/(Al) GaAs quantum dots. *Physical Review B*, *65*(19), 195315.

[22] Ramsay, A. J. (2010). A review of the coherent optical control of the exciton and spin states of semiconductor quantum dots. *Semiconductor Science and Technology*, *25*(10), 103001.

[23] Lodahl, P., Mahmoodian, S., & Stobbe, S. (2015). Interfacing single photons and single quantum dots with photonic nanostructures. *Reviews of Modern Physics*, *87*(2), 347.

[24] Matthiesen, C., Vamivakas, A. N., & Atatüre, M. (2012). Subnatural linewidth single photons from a quantum dot. *Physical Review Letters*, *108*(9), 093602.

[25] Nguyen, H. S., Sallen, G., Voisin, C., Roussignol, P., Diederichs, C., & Cassabois, G. (2011). Ultra-coherent single photon source. *Applied Physics Letters*, *99*(26), 261904.

[26] Hecht, E. (2014). *Optics* (4th ed.). Pearson Education Limited.

[27] Loudon, R. (2000). *The quantum theory of light*. OUP Oxford.

[28] Phillips, C. L., Brash, A. J., McCutcheon, D. P., Iles-Smith, J., Clarke, E., Royall, B., ... & Nazir, A. (2020). Photon Statistics of Filtered Resonance Fluorescence. *arXiv preprint arXiv:2002.08192*.

[29] Hinchliff, J. (2018). *Nuclear spin control and manipulation in self-assembled quantum dots* (Doctoral dissertation, University of Bristol, Bristol, England).

[30] Sun, Z., Delteil, A., Faelt, S., & Imamoğlu, A. (2016). Measurement of spin coherence using Raman scattering. *Physical Review B*, *93*(24), 241302.

[31] Stockill, R., Le Gall, C., Matthiesen, C., Huthmacher, L., Clarke, E., Hugues, M., & Atatüre, M. (2016). Quantum dot spin coherence governed by a strained nuclear environment. *Nature communications*, *7*, 12745.

[32] Belykh, V. V., Greilich, A., Yakovlev, D. R., Yacob, M., Reithmaier, J. P., Benyoucef, M., & Bayer, M. (2015). Electron and hole g factors in InAs/InAlGaAs self-assembled quantum dots emitting at telecom wavelengths. *Physical Review B*, *92*(16), 165307.

[33] Besombes, L., Kheng, K., Marsal, L., & Mariette, H. (2001). Acoustic phonon broadening mechanism in single quantum dot emission. *Physical Review B*, *63*(15), 155307.

[34] Kaer, P., & Mørk, J. (2014). Decoherence in semiconductor cavity QED systems due to phonon couplings. *Physical Review B*, *90*(3), 035312.

[35] Reigue, A., Iles-Smith, J., Lux, F., Monniello, L., Bernard, M., Margaillan, F., ... & Hostein, R. (2017). Probing electron-phonon interaction through two-photon interference in resonantly driven semiconductor quantum dots. *Physical Review Letters*, *118*(23), 233602.

[36] Hu, X., de Sousa, R., & Sarma, S. D. (2002). Decoherence and dephasing in spin-based solid state quantum computers. In *Foundations Of Quantum Mechanics In The Light Of New Technology: ISQM—Tokyo'01* (pp. 3-11).

[37] Somaschi, N., Giesz, V., De Santis, L., Loredo, J. C., Almeida, M. P., Hornecker, G., ... & Gómez, C. (2016). Near-optimal single-photon sources in the solid state. *Nature Photonics*, *10*(5), 340-345.

[38] Wang, H., Duan, Z. C., Li, Y. H., Chen, S., Li, J. P., He, Y. M., ... & Schneider, C. (2016). Near-transform-limited single photons from an efficient solid-state quantum emitter. *Physical Review Letters*, *116*(21), 213601.

[39] Ramsay, A. J., Gopal, A. V., Gauger, E. M., Nazir, A., Lovett, B. W., Fox, A. M., & Skolnick, M. S. (2010). Damping of exciton rabi rotations by acoustic phonons in optically excited InGaAs/GaAs quantum dots. *Physical review letters*, *104*(1), 017402.

[40] Iles-Smith, J., McCutcheon, D., Nazir, A. and Mørk, J. (2017). Phonon scattering inhibits simultaneous near-unity efficiency and indistinguishability in semiconductor single-photon sources. *Nature Photonics*, 11(8), pp.521-526.

[41] Brash, A., Iles-Smith, J., Phillips, C., McCutcheon, D., O'Hara, J., Clarke, E., Royall, B., Wilson, L., Mørk, J., Skolnick, M., Fox, A. and Nazir, A. (2019). Light Scattering from Solid-State Quantum Emitters: Beyond the Atomic Picture. *Physical Review Letters*, 123(16), 167403.

[42] Koong, Z., Scerri, D., Rambach, M., Santana, T., Park, S., Song, J., Gauger, E. and Gerardot, B. (2019). Fundamental Limits to Coherent Photon Generation with Solid-State Atomlike Transitions. *Physical Review Letters*, 123(16), 167402.

[43] Nazir, A., & McCutcheon, D. P. (2016). Modelling exciton–phonon interactions in optically driven quantum dots. *Journal of Physics: Condensed Matter*, *28*(10), 103002.

[44] Chen, P., Piermarocchi, C., Sham, L. J., Gammon, D., & Steel, D. G. (2004). Theory of quantum optical control of a single spin in a quantum dot. *Physical Review B*, *69*(7), 075320.

[45] Pryor, C. E., & Flatté, M. E. (2006). Predicted ultrafast single-qubit operations in semiconductor quantum dots. *Applied physics letters*, *88*(23), 233108.

[46] Economou, S. E., Sham, L. J., Wu, Y., & Steel, D. G. (2006). Proposal for optical U (1) rotations of electron spin trapped in a quantum dot. *Physical Review B*, *74*(20), 205415.

[47] Clark, S. M., Fu, K. M. C., Ladd, T. D., & Yamamoto, Y. (2007). Quantum computers based on electron spins controlled by ultrafast off-resonant single optical pulses. *Physical Review Letters*, *99*(4), 040501.

[48] Petta, J. R., Johnson, A. C., Taylor, J. M., Laird, E. A., Yacoby, A., Lukin, M. D., ... & Gossard, A. C. (2005). Coherent manipulation of coupled electron spins in semiconductor quantum dots. *Science*, *309*(5744), 2180-2184.

[49] De Greve, K., Press, D., McMahon, P. L., & Yamamoto, Y. (2013). Ultrafast optical control of individual quantum dot spin qubits. *Reports on Progress in physics*, *76*(9), 092501.

[50] Press, D., Ladd, T. D., Zhang, B., & Yamamoto, Y. (2008). Complete quantum control of a single quantum dot spin using ultrafast optical pulses. *Nature*, *456*(7219), 218-221.

[51] Fleischhauer, M., Imamoglu, A., & Marangos, J. P. (2005). Electromagnetically induced transparency: Optics in coherent media. *Reviews of modern physics*, *77*(2), 633.

[52] Vitanov, N. V., Rangelov, A. A., Shore, B. W., & Bergmann, K. (2017). Stimulated Raman adiabatic passage in physics, chemistry, and beyond. *Reviews of Modern Physics*, *89*(1), 015006.

[53] Atatüre, M., Dreiser, J., Badolato, A., Högele, A., Karrai, K., & Imamoglu, A. (2006). Quantum-dot spin-state preparation with near-unity fidelity. *Science*, *312*(5773), 551-553.

[54] Rabi, I. I., Millman, S., Kusch, P., & Zacharias, J. R. (1939). The molecular beam resonance method for measuring nuclear magnetic moments. the magnetic moments of li 6 3, li 7 3 and f 19 9. *Physical review*, *55*(6), 526.

[55] Ding, D., Appel, M. H., Javadi, A., Zhou, X., Löbl, M. C., Söllner, I., ... & Wieck, A. D. (2019). Coherent optical control of a quantum-dot spin-qubit in a waveguide-based spin-photon interface. *Physical Review Applied*, *11*(3), 031002.

[56] Carter, S. G., Shabaev, A., Economou, S. E., Kennedy, T. A., Bracker, A. S., & Reinecke, T. L. (2009). Directing nuclear spin flips in InAs quantum dots using detuned optical pulse trains. *Physical review letters*, *102*(16), 167403.

[57] Greilich, A., Yakovlev, D. R., Shabaev, A., Efros, A. L., Yugova, I. A., Oulton, R., ... & Bayer, M. (2006). Mode locking of electron spin coherences in singly charged quantum dots. *Science*, *313*(5785), 341-345.

[58] De Greve, K. (2012). *Towards solid-state quantum repeaters: ultrafast, coherent optical control and spin-photon entanglement in charged InAs quantum dots.* (Doctoral dissertation, Stanford University, Stanford, United States).